Footprint: A look at seismic acquisition geometries using 3D prestack depth migration.

Gary F. Margrave

ABSTRACT

The acquisition footprint of a 3D survey refers to any imprint or modulation of the amplitude and phase of the final migrated depth image that is directly attributable to the survey geometry, that is, the positions of sources and receivers. Since processing algorithms differ in their ability to deal with geometric problems, the footprint is generally also a function of the processing flow. This paper examines some of the factors affecting footprint for a typical land 3D geometry when imaged with prestack source-record migration. As a preliminary, a brief overview is given of some of the sampling issues concerning possible spatial aliasing with respect to the sampling intervals of receivers, receiver lines, sources, and source lines. The footprint is then examined through a numerical simulation that consists of (1) image-source modeling of the reflection response of a uniform horizontal reflector, (2) prestack depth migration of each source record, and (3) summation of the migrated source records with and without illumination compensation. Two different models of illumination estimation are examined. One is the direct thresholding of the rectified migration response for each source record and the other is the thresholding of the rectified, normalized crosscorrelation of the source and receiver functions. Illumination compensation was undertaken by dividing the source-record stack by the corresponding stack of illumination estimates. Simulation results for both PP and PS recording are shown. Some general conclusions are: (1) some form of footprint is unavoidable, (2) direct stacking of migrated source record without illumination compensation leaves a strong aperture imprint (3) illumination compensation lessens the aperture imprint but can worsen the imprint of the geometry (4) the spatial aliasing due to course source and receiver line spacings is roughly compensated if the lines are orthogonal (5) the geometry is very effective against both random and coherent noise although the latter is more problematic (6) strong levels of coherent noise dramatically worsen the footprint effect. The Matlab script files for this simulation are released with this paper and are intended to allow exploration of parameter interactions that are beyond the scope of this introductory paper.

INTRODUCTION

A frequent observation from experienced seismic interpreters is that the acquisition geometry of a seismic survey can leave an imprint on the final seismic image. Such imprints are often called the acquisition footprint and that term is used here. On the simplest level, this is an obvious, almost trivial observation. Of course the finite spatial and temporal apertures impose limits on the resulting seismic image. Of course, the sampling grids for sources and receivers have an impact on resolution. However, there are much more subtle effects that are not so easily recognized or anticipated. For example, the source and receiver lattices (i.e. the set of all source or receiver locations) are generally different from each other and have different aliasing and resolution properties. Furthermore, the particular data processing algorithms used can interact with

these sampling lattices in complicated, algorithmically specific ways. So we would expect conventional processing followed by poststack migration to have a different footprint that prestack migration. Moreover, since there are many different prestack depth migration methods, we should expect each one to have a different footprint.

The situation in 3D is potentially more difficult, and has greater impact, because 3D lattices are more likely to be sub-optimal than 2D. In the 2D case, the lattices are 1D linear arrays and the receiver lattice is almost always regular and sufficiently dense. The source lattice is more problematic, with missed source locations and insufficient density being frequent occurrences. This is known to cause fold and image quality variations that can be considered as a 2D footprint. In 3D, sufficiently dense sampling to avoid aliasing is extremely difficult to achieve because the lattices are now 2D and require a dense array over an area rather than a line. The cost of adequate spatial sampling for both sources and receivers is usually prohibitive and various compromise strategies have evolved.

This paper recounts the initial steps in an investigation of the footprint resulting from prestack depth migration using typical 3D land acquisition strategies. This is very relevant to the research priorities of our imaging group as we develop advanced imaging algorithms and move them into 3D. Since we hope to develop methods that improve the quality of land 3D seismic images, we need to understand what strategies are required to deal with the source and receiver lattices that are typically employed. This paper begins with a theoretical discussion of sampling issues in 3D prestack depth migration. Then the construction of a Matlab code that simulates an idealized 3D prestack depth migration is described. Two different schemes for calculating illumination are presented and the use of illumination estimates to normalize a 3D image is discussed. Finally a variety of graphical displays from a series of tests for both PP and PS migrations are presented.

MIGRATION THEORY AND SAMPLING ISSUES

Figure 1 shows a typical 3D acquisition geometry for a land seismic survey. The horizontal lines with red symbols denote source locations and the vertical lines with blue symbols are receiver locations. The set of all red symbols is the source lattice while all blue symbols form the receiver lattice. The sampling compromise is that the receivers are laid out in dense linear arrays along *receiver lines* while the interval between receiver lines is relatively coarse. The source locations are also laid out in a similar fashion except that the source lines are orthogonal to the receiver lines. Thus the receiver sampling is excellent in a direction which is chosen as the x-axis and very poor in the y direction. In contrast, the source sampling is excellent in y but poor in x. Such layouts have been called *symmetric sampling* by Vermeer (1998) who considers them to have optimal properties. It is obviously hoped that this orthogonal compromise will have beneficial effects in that the source and receiver lattices will somehow compensate for each others shortcomings. Three different variations of the geometry of Figure 1 will be considered in this paper. Denote the receiver spacing as δr, the receiver line spacing as δrl, the source spacing as δs and the source line spacing as δsl. When $\delta r = \delta rl = \delta s = \delta sl$ the geometry will be called *complete*. When $\delta r = \delta rl = \delta s$ but $\delta sl > \delta s$ the geometry will be called *source reduced*. When $\delta r = \delta s$ but $\delta rl = \delta sl > \delta s = \delta r$ the geometry will be called *source-receiver reduced*. Typically the receiver and source spacings will be 10 m and the reduced line spacings will be 100 m .
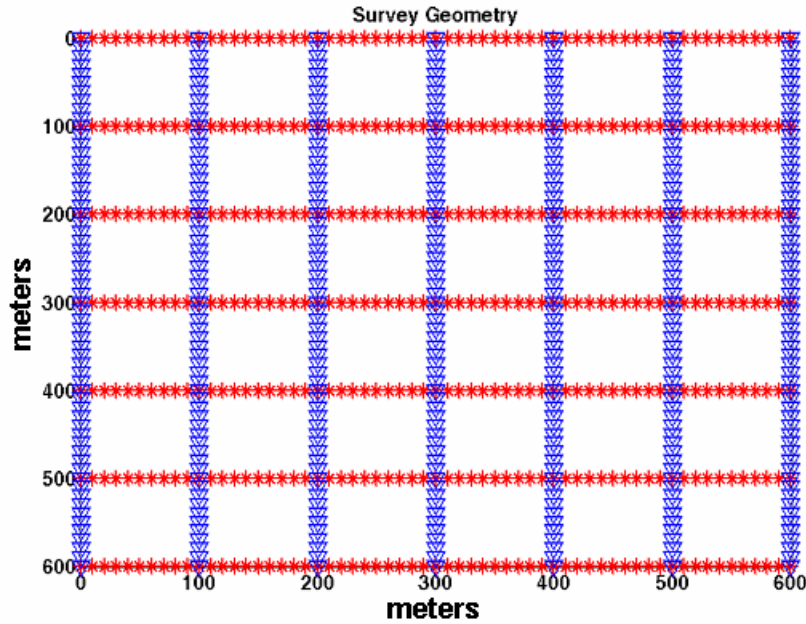
Figure 1. The nominal geometry for the experiments reported here. The blue lines are the receiver lines and the red lines are the source lines. This is called the source-receiver reduced geometry. When the additional receiver lines are in-filled to make the receiver line spacing equal the receiver spacing, the result is called the source-reduced geometry. When the sources are also in-filled, the result is called the complete geometry.

The prestack depth migration algorithm chosen for simulation here is source-record migration. In this scheme, each individual source record is migrated as an independent experiment and then all migrated source records are stacked (summed) together. This is a common scheme and has the virtue that the migration process is nicely restricted to subsets of the total dataset, and thus has obvious potential for distribution of the computing load across a parallel computation cluster. The basic paradigm of source-record migration is that the reflection coefficient, as a function of lateral position, is estimated at each depth from the ratio of two fields

$$r_j(x,y,z) = \frac{1}{n_\omega} \sum_k \frac{U_j(x,y,z,\omega_k)}{D_j(x,y,z,\omega_k)} \tag{1}$$

where j is a source index, n_ω is the number of frequency samples, U_j is the upward scattered, or reflected, field, D_j is the downward traveling, or incident field, ω_k is a discrete temporal frequency, and the summation is over frequency. While equation (1) is the usual definition of reflection coefficient, in practice, a stabilized version is used (to avoid possible division by zero) given by

$$r_j(x,y,z) = \frac{1}{n_\omega} \sum_k \frac{U_j(x,y,z,\omega_k)\bar{D}_j(x,y,z,\omega_k)}{D_j(x,y,z,\omega_k)\bar{D}_j(x,y,z,\omega_k)+\varepsilon} \qquad (2)$$

where the overbar denotes complex conjugation, and ε is a small positive number. The field U_j is calculated by downward extrapolation of the recorded data through an estimated background velocity model. The field D_j is calculated by downward extrapolation of a mathematical model of the source for this particular source record. Both equations (1) and (2) are called *deconvolution imaging conditions* because the appearance of the source model in the denominator effectively deconvolves the source signature from the final estimate. While theoretically preferable, a deconvolution imaging condition can cause unacceptable noise amplification and therefore the *crosscorrelation imaging condition* given by

$$r_j(x,y,z) = \frac{1}{n_\omega} \sum_k U_j(x,y,z,\omega_k)\bar{D}_j(x,y,z,\omega_k) \qquad (3)$$

is sometimes preferred. Though equation (3) does not correct for source signature or for geometric spreading it is still very commonly used for its gentle treatment of background noise. (See the discussion in "Results" about random noise for more information.

Regardless which imaging condition is used, the final prestack depth migration image is calculated as a normalized summation over all available sources

$$r(x,y,z) = \frac{\sum_j r_j(x,y,z)}{I(x,y,z)} \qquad (4)$$

where the normalization term $I(x,y,z)$ is so-named to suggest its interpretation as an illumination estimate. Two different illumination estimates will be investigated here, given by equations (20) and (22), and will be described below.

An essential feature of this method is the wavefield extrapolation process. In the simplest possible method, which will be completely sufficient for this paper, the wavefield, either U_j or D_j, at depth $z+\Delta z$ is calculated from that at depth z by a phase shift operation in the Fourier domain. For U_j this is

$$U_j(x,y,z+\Delta z,\omega) = \int_{\mathbb{R}^2} \hat{U}_j(k_x,k_y,\omega,z)\hat{W}(k_x,k_y,\omega,\Delta z)e^{i(k_x x+k_y y)}dk_x dk_y \quad (5)$$

and there is a corresponding formula for D_j. In equation (5), $\hat{U}_j$ is the 2D Fourier transform of U_j, (k_x,k_y) are the Fourier dual variables (wavenumbers) corresponding to (x,y), and $\hat{W}$ is the wavefield extrapolator in the Fourier domain given by

$$\hat{W}\left(k_x,k_y,\omega,\Delta z\right) = \begin{cases} \exp\left(i\Delta z\sqrt{\omega^2 v^{-2} - k_x^2 - k_y^2}\right), |\omega| > v\sqrt{k_x^2 + k_y^2} \\ \exp\left(-\Delta z\sqrt{k_x^2 + k_y^2 - \omega^2 v^{-2}}\right), |\omega| \le v\sqrt{k_x^2 + k_y^2} \end{cases} \tag{6}$$

where v is the constant background wavespeed appropriate for the depth interval $[z, z+\Delta z]$. The first form of the wavefield extrapolator, valid for $|\omega| > v\sqrt{k_x^2 + k_y^2}$, describes the behavior of propagating waves, while the second form describes evanescent waves. The phenomenon of evanescence is central to considerations here because the exponential damping of wavenumbers for which $\sqrt{k_x^2 + k_y^2} > |\omega| v^{-1}$ forms a natural spectral bandlimiting in the spatial frequencies. Thus, ideally, we would like spatial sample intervals, δx and δy, such that

$$\frac{\pi}{\delta x} = \frac{\pi}{\delta y} > \frac{\omega_{max}}{v} \tag{7}$$

Solving for the sample intervals and converting to $f_{max} = \omega_{max}/2\pi$ gives the condition

$$\delta x, \delta y < \frac{v}{2 f_{max}} \tag{8}$$

by which it is meant that both spatial sample intervals should satisfy this inequality. In the simulations to be described below, the usual maximum frequency was $f_{max} = 60\,\text{Hz}$ and $v = 3000\,\text{m/s}$, which leads to the conclusion that both sample intervals should be smaller than 25 m. Equivalently, from (7) we can say that wavenumbers from zero to $\omega_{max} v^{-1} = \pi/25 \approx .126\,\text{m}^{-1}$ are expected to contain reflection signal.
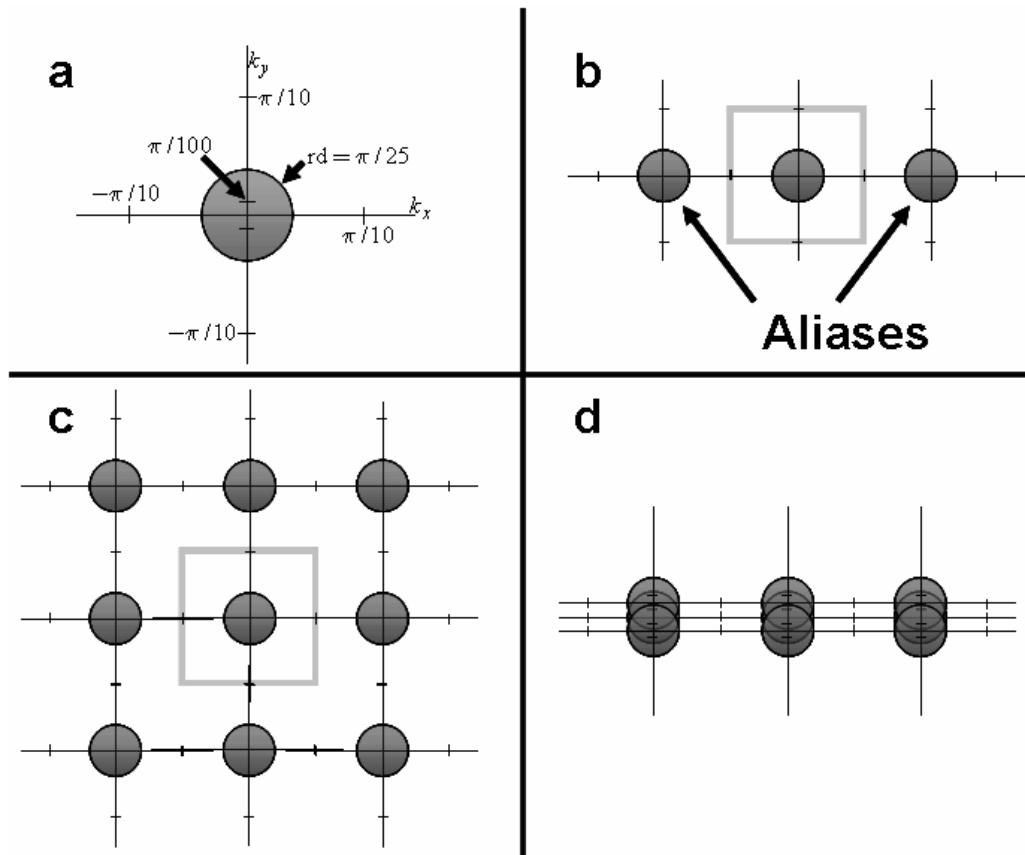
Figure 2. (a) The spectral setting in the analog setting as described in the text. The circle represents the width of the propagating wavelet spectrum for 60 Hz and a velocity of 3000 m/s. The various tic marks indicate potential Nyquist wavenumbers, of the form $\pm\pi/\delta$, where δ is a sample interval in meters. (b) The spectrum in (a) after sampling in x at 10 meter intervals. The box indicates the original spectrum while the circles to the left and right are the first two, of infinitely many, aliases. (c) The spectrum in (b) after sampling in y at 10 m intervals. (d) The spectrum in (b) after sampling in y at 100 m intervals. Only the first two aliases in either direction are shown.

For the migration of a single source, the sampling issues are clear. Figure 2a shows a symbolic spectral plot representing the ideal unsampled (analog) case. The coordinate axes are the two horizontal wavenumbers and the circle around the origin has a radius of $\pi/25\,\mathrm{m}^{-1}$ representing the expected reflection data. Also shown are tic marks on the k_x and k_y axes at $\pm\pi/10$ representing the Nyquist wavenumbers for 10 meter sampling and on the k_y axis only are tic marks at $\pm\pi/100$ representing the Nyquist for 100 meter sampling. Consider first the effect of sampling in x only at $\delta x = 10\,\mathrm{m}$. As is well known, this introduces spectral replicas along k_x, called *aliases*, at intervals of $\pm 2n\pi/10$ where *n* is a positive integer. The first two aliases are shown in Figure 2b. Since the aliases of the signal circle do not intersect with the original, this circumstance is said to be *unaliased*. Next consider sampling in the y direction at $\delta y = 10\,\mathrm{m}$. This introduces spectral aliases in the k_y direction as shown in Figure 2c. There is still no aliasing. Finally consider sampling in the y direction at $\delta y = 100\,\mathrm{m}$, corresponding to

the interval between receiver lines in the receiver-reduced geometry, and the spectral picture becomes aliased as shown in Figure 2d.

At first thought, the aliasing of Figure 2d seems a hopeless circumstance; yet, the corresponding acquisition geometry has been used successfully many times. Since the source-reduced geometry is orthogonal to the receiver reduced geometry, there is some reason to hope that the composite image, formed by stacking all migrated source records, might somehow be less hopelessly aliased. While a complete analysis of the effect of these sampling lattices in prestack depth migration is presently elusive, several lines of reasoning suggest themselves. First, one might appeal to source-receiver reciprocity arguments. While the full vector reciprocity relationship for elastic wavefields are sufficiently complicated that they are difficult to interpret, there are simple, approximate scalar reciprocity arguments in common use that do help. For example, it is well known that common receiver gathers are very similar in all respects to common source gathers. In fact, a common migration algorithm that gives very similar results to source-record migration treats common source and common receiver gathers as completely equivalent at all algorithm steps. Second, the conventional process of NMO removal, stack, and post-stack migration admits a simple argument showing that the final image wavenumbers come in equal parts from sources and receivers. To understand this point, let $\psi(s,r,\omega)$ be a single frequency from a 2D wavefield with sources at coordinates s and receivers at r. Furthermore, assume that NMO has already been removed. Define midpoint, m, and half-offset, h, coordinates via $m = (s+r)/2$ and $h = (r-s)/2$, then represent stacking as integration over h

$$\psi_{stk}(m,\omega) = \int_{\mathbb{R}} \psi(m-h, m+h, \omega)\,dh \tag{9}$$

Now represent $\psi(s,r,\omega)$ in terms of its inverse Fourier transform

$$\psi(s,r,\omega) = \int_{\mathbb{R}^2} \hat{\psi}(k_s, k_r, \omega) e^{i(k_s s + k_r r)}\,dk_s dk_r \tag{10}$$

and insert equation (10) into equation (9) to get

$$\psi_{stk}(m,\omega) = \int_{\mathbb{R}} \int_{\mathbb{R}^2} \hat{\psi}(k_s, k_r, \omega) e^{i(k_s(m-h) + k_r(m+h))}\,dk_s dk_r dh \tag{11}$$

which can be re-arranged to give

$$\psi_{stk}(m,\omega) = \int_{\mathbb{R}} \int_{\mathbb{R}^2} \hat{\psi}(k_s, k_r, \omega) e^{i((k_s+k_r)m + (k_r-k_s)h)}\,dk_s dk_r dh, \tag{12}$$

the h integration gives a delta function and we get

$$\psi_{stk}(m,\omega) = 2\pi \int_{\mathbb{R}^2} \hat{\psi}(k_s, k_r, \omega) \delta(k_r - k_s) e^{i(k_s+k_r)m}\,dk_s dk_r. \tag{13}$$

From here we can do either the k_s or the k_r integral and the delta function forces $k_s = k_r$. The following conclusions are immediate: (a) the diagonal entries (i.e. $k_r = k_s$)

of $\hat{\psi}(k_s, k_r, \omega)$ form the spectrum of ψ_{stk}, (b) the wavenumbers, k_m, corresponding to midpoint come in equal part from k_s and k_r, (c) since $k_m = 2k_r = 2k_s$ the bandwidth in the image is double that in source or receiver gathers. Though this was developed in 2D for convenience, the conclusions also hold for 3D.

The argument just given actually suffices for the experiment to be described in this paper because conventional processing (NMO removal, stack, poststack migration) is essentially equivalent to prestack migration for horizontal, uniform reflectors. However, it is not a complete description of the spectral properties of a general prestack depth migration. That more complete theory will have to wait. For now, a few comments upon the implications of sampling in the conventional processing argument are warranted. First, "symmetric" sampling (Vermeer, 1990, 1998), where source and receiver lattices are identical (and in 3D orthogonal), seems optimal because of the equal status of the alternate gathers. In the 2D case, if $\delta s = 2\delta r$ (a common shooting strategy), then only the lower half of the k_m spectrum is formed from unaliased data while the upper half receives unaliased contributions from receivers but aliased from sources. A reasonable expectation for 3D geometries is that, with the source-receiver reduced geometry (described at the beginning of this section, see also Figure 1) the k_x wavenumbers of the final image receive unaliased contributions from receivers and aliased from sources while the k_y wavenumbers are unaliased from the sources but aliased from the receivers. Since it is generally the case that aliased data migrates incoherently, a reasonable expectation is that the source-receiver reduced geometry will perform acceptably provided that there is sufficient illumination to overcome noise.

BUILDING THE NUMERICAL SIMULATION CODE

Since the issues surrounding the footprint are complex and highly dependent upon a great many variables, a numerical simulation code seems like a reasonable initial investigative tool. The simulation is written in Matlab in the form of a series of scripts and is available to interested persons at sponsor companies; however, it is not intended to be a user-friendly, mass-release product. At present, the simulation is limited to orthogonal source and receiver lines. The aperture, receiver spacing, receiver line spacing, source spacing, and source line spacing are all modifiable parameters. The earth model is limited to a single horizontal reflector, at user specified depth, with constant velocity above. At present, the reflection coefficient is limited to a constant value independent of incidence angle. While obviously unphysical especially in the PS case, this featureless reflector means that any variation seen in the migrated image is a footprint effect.

The forward modeled data are created in the temporal frequency domain by a simple modeling technique. For PP data, an image source is placed beneath the reflector at a depth equal to twice the reflector depth and the data is then created as a simple frequency domain Green's function of the form

$$U_{j;PP}(x,y,z=0) = c\,s(\omega)\frac{e^{-i\omega\rho/v_p}}{\rho} \qquad (14)$$

where j denotes a particular source at $(x_j, y_j, 0)$, c is the reflection coefficient, v_p is the p-wave velocity,

$$\rho = \sqrt{4z_0^2 + (x-x_j)^2 + (y-y_j)^2}\,, \qquad (15)$$

and $s(\omega)$ is the spectral shape function of the source. In all simulations here $s(\omega)$ was taken as a raised cosine function extending from prescribed values of ω_{min} to ω_{max}.

For PS data, raytracing software is used to determine the location of the PS conversion point and then the distances from source to conversion point, ρ_1, and receiver to conversion point, ρ_2, are calculated. Using this information equation (14) is modified to

$$U_{j;PS}(x,y,z=0) = c\,s(\omega)\frac{e^{-i\omega(\rho_1/v_p + \rho_2/v_s)}}{\rho_1 + \rho_2}\,. \qquad (16)$$

This data model is very approximate but at least it gets the correct traveltimes and approximately the correct spreading. A more accurate model would avoid the conversion point calculation (because it is correct only in the high-frequency limit) and angle and position dependent reflection coefficients. Better modeling is under investigation.

Both random and coherent noises are simulated. For random noise, a "noise-to-signal" ratio, η, is specified as the ratio of random noise to peak signal strength at the dominant frequency. Thus each frequency gets a unique random number field but the power of this field is independent of frequency. For coherent noise, a linear noise train (non-dispersive) is available. The strength of the noise and its velocity are parameters and it's spectral shape function is prescribed independently of the shape function for the signal. The noise is modeled as

$$U_{j;surfnoise}(x,y,z=0) = a_{surf}\,s_{surf}(\omega)\frac{e^{-i2\omega h/v_0}}{\sqrt{2h}} \qquad (17)$$

where a_{surf} is the noise strength, $s_{surf}(\omega)$ is the spectral shape function, h is the source-receiver half-offset, and v_0 is the velocity of the noise.

The modeling and migration are done simultaneously frequency-by-frequency and source-by-source. In general, only 1/4 of the sources need to be explicitly calculated because the others follow from symmetry operations. Implementation of the imaging condition, equation (2), at the reflector requires three preliminary calculations:

i.   The receiver data are regularized by some sort of interpolation process to fill in missing receivers between receiver lines. After interpolation, the receiver data are available on a square grid whose spacing is the receiver interval.

ii.   The receiver data are extrapolated down to the reflector using equation (5).

iii.   The source must be forward modeled to the reflector.

Regarding issue (i) there are many possibilities and the solution chosen here was a simple Fourier-domain interpolation that does not unalias data. For issue number (ii) a simple constant velocity phase shift is used. The phase shift velocity is v_p for p-wave data and v_s for s-wave data. Finally, for point (iii) the source is directly forward modeled at the reflector using the Green's function

$$D_{j;PP}(x, y, z = z_0) = s(\omega) \frac{e^{-i\omega\rho_0/v_p}}{\rho_0} \tag{18}$$

where

$$\rho_0 = \sqrt{z_0^2 + (x - x_j)^2 + (y - y_j)^2} \,. \tag{19}$$

The same source model works for both PP and PS data.

As each source is completely modeled and migrated, its individual frequencies are summed (as in equation (2)) and the total source is then summed into the output volume. As this happens, two alternate estimates of *illumination* are also computed. These are two possible generalizations of the concept of stacking fold. In principle, each source record can provide a reflectivity estimate at every point on the reflector, since scattered energy goes everywhere. However, in practice, the estimates are only reliable if come from a sufficiently strong signal. This suggests that the strength of r_j itself as estimated from equation (2) might be a good indicator. This motivates the first illumination estimate

$$I_{r;j}(x, y, z) = \begin{cases} 1.0 \ldots |r(x, y, z)| > \mu r_{\max} \\ \dfrac{|r(x, y, z)|}{\mu r_{\max}} \ldots \text{otherwise} \end{cases} \tag{20}$$

where μ is an adjustable parameter presently taken to be around 0.4, and $r_{\max} = \max(|r_j(x, y, z)|)$. The name $I_{r;j}$ is meant to indicate that this estimate comes from the reflectivity estimate for the jth source. The form of equation (20) is such that the illumination has a value of unity whenever the absolute value of the reflectivity estimate exceeds μ times the maximum absolute value of the reflectivity found anywhere in the migrated source record. Otherwise, it tapers smoothly to zero. This definition of illumination is similar to that proposed by Rickett (2003) who defines illumination as the

result of a prestack migration of a synthetic dataset divided by the actual model reflectivity. Since the model reflectivity is a constant in this case, the result seems similar. However, Rickett (2003) did not propose thresholding and his definition could well exceed unity or be negative.

The second choice investigated as an illumination measure is to use the normalized crosscorrelation of the source and receiver wavefields as estimated at each depth. This crosscorrelation is defined as

$$cc_j(x,y,z) = \sum_k \frac{U_j(x,y,z,\omega_k)\bar{D}_j(x,y,z,\omega_k)}{\sqrt{U_j^2(x,y,z,\omega_k)D_j^2(x,y,z,\omega_k)}+\varepsilon} \tag{21}$$

where $U_j^2 = U_j\bar{U}_j$ and similarly for D_j^2. Though similar to the reflectivity estimate in equation (2), this is not the same. Then a crosscorrelation-based illumination estimate is defined in a similar way as before with

$$I_{cc;j}(x,y,z) = \begin{cases} 1.0 \ldots |cc(x,y,z)| > \nu cc_{\max} \\ \dfrac{|cc(x,y,z)|}{\nu cc_{\max}} \ldots \text{otherwise} \end{cases} \tag{22}$$

where again a threshold, ν, must be chosen, with $\nu = .9$ having been used in this study.

As each source is modeled and migrated, the two different illumination functions are also calculated. Along with the stacks of the migrated sources, two different illumination function stacks are also made. An illumination compensated reflectivity estimate then corresponds to

$$r_I(x,y,z) = \frac{\sum_j r_j}{\sum_j I_{r;j}} \tag{23}$$

or

$$r_{Icc}(x,y,z) = \frac{\sum_j r_j}{\sum_j I_{cc;j}}. \tag{24}$$

Four scripts have been written in total and are available to CREWES sponsors. The scripts *footprintPP.m* and *footprintPS.m* perform the tasks just discussed and make plots. However the displays are limited to the final results corresponding to equations (23) and (24) plus the uncompensated reflectivity stack and the two illumination stacks. Scripts *illumination_functionsPP.m* and *illumination_functionsPS.m* are similar to the other scripts except that only four sources are explicitly modeled and a great many plots of intermediate results are possible.

RESULTS

In all of the results presented in this section, there was a single horizontal reflector at 500 m depth, with a constant reflection coefficient of 0.1 for both PP and PS. The p-wave velocity was 3000 m/s and the s-wave velocity was 1500 m/s. The survey aperture was 600 meters in each direction, the receiver and source spacings were 10 meters, and, for the reduced geometries, the receiver and source line spacings were 100 meters. The source bandwidth was taken to be from 10-60 Hz with a raised-cosine spectral-shaping function (see equation (14)). The figures shown here are all direct outputs from the scripts and can be recreated by the reader with access to Matlab.

As a first example of the results from these scripts, Figures 3-6 show the results for the complete geometry in both the PP and PS cases. While the complete geometry would never be used for economic reasons, it is instructive to examine the results as limiting cases. In Figure 3a, the stack of the migrated source records is shown, normalized by the number of sources (3600). Although the actual reflection coefficient is a constant across the aperture of the survey, the estimate shows strong variation that is directly related to the illumination issue. At this time, the modeling algorithm is not sufficiently realistic to expect the precise reflection coefficient to be estimated. A more realistic expectation is that the bet result will be off by a constant scale factor. Clearly, Figure 3a shows an estimate that is incorrect by much more than a constant scale factor. This is an example of a footprint. In Figure 3b is the illumination stack for the I_r estimate of equation (20). Its maximum value is about 3600 but that tapers off to well less than 1000 near the corners of the survey. Figure 3c shows the illumination normalized stack (equation (23)). This is the result of dividing Figure 3a by 3b and then multiplying by 3600 (because 3a was normalized by 3600). The illumination normalization has broadened the "plateau" of the reflectivity estimate but at the expense of introducing a roughly square artifact in the footprint. In Figure 4, the same displays are show except for the case of PS migration. Since the PS conversion point is closer to the receiver than the PP conversion point, the reflectivity estimate is flatter over the central region. This is similar to the effect seen in a PP survey for a shallower reflector (not shown). The illumination compensated PS estimate (Figure 4c) shows a footprint but a satisfyingly large central plateau. Figures 5 and 6 are similar to 3 and 4 except that the I_{cc} illumination estimate was used. There seems to be a slight preference for I_{cc} on PP and I_r on PS but this could simply be due to suboptimal choices for the thresholds in equations (20) and(22). This is a subject for future investigation.
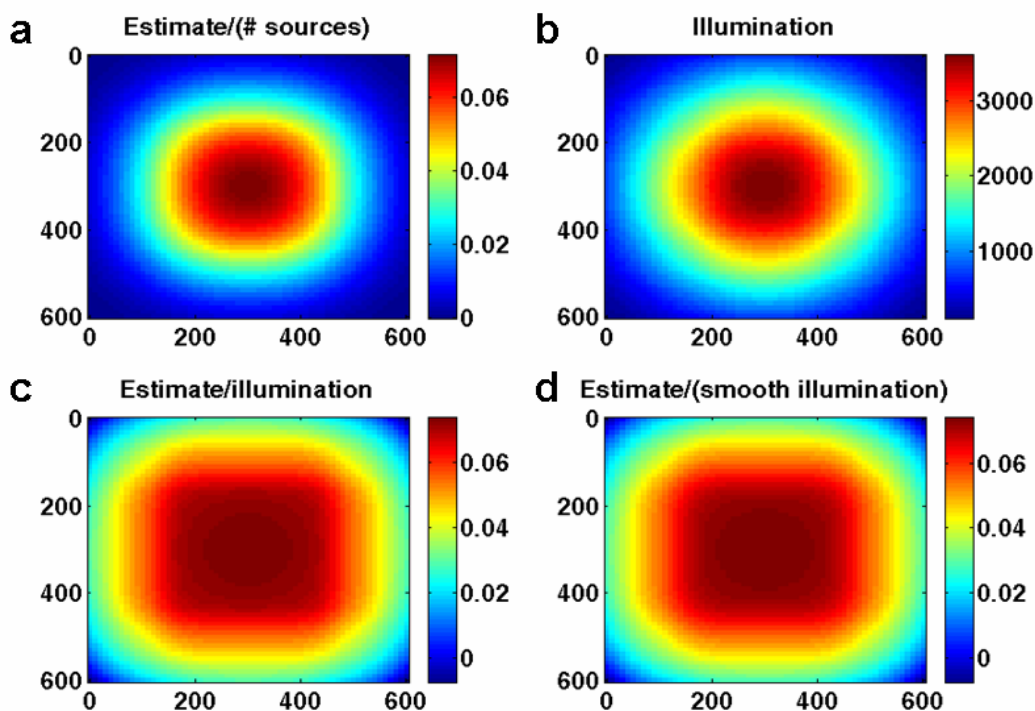
Figure 3. The results of a PP experiment using the complete geometry and no coherent or random noise. The illumination estimates are I_r (equation (20)). (a) The raw reflectivity estimate or direct stack of the migrated sources normalized by the number of sources. (b) The illumination stack. (c) The illumination compensated reflectivity estimate. (d) The illumination compensated reflectivity estimate using a smoothed illumination stack.
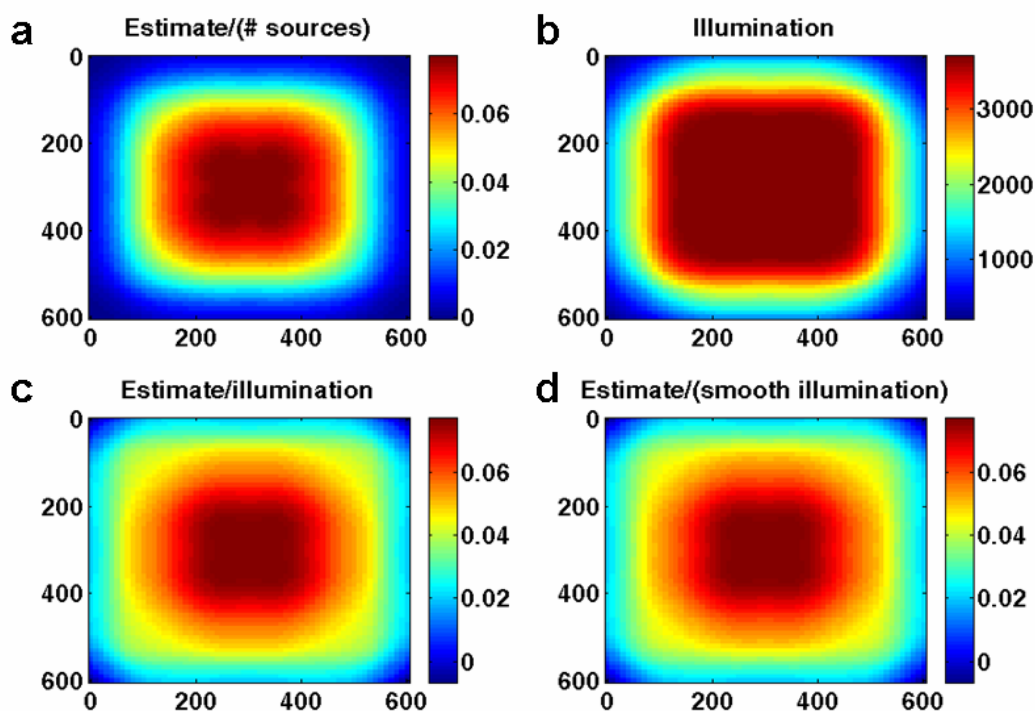
Figure 4. Similar to Figure 3 except that the PS algorithm was used.
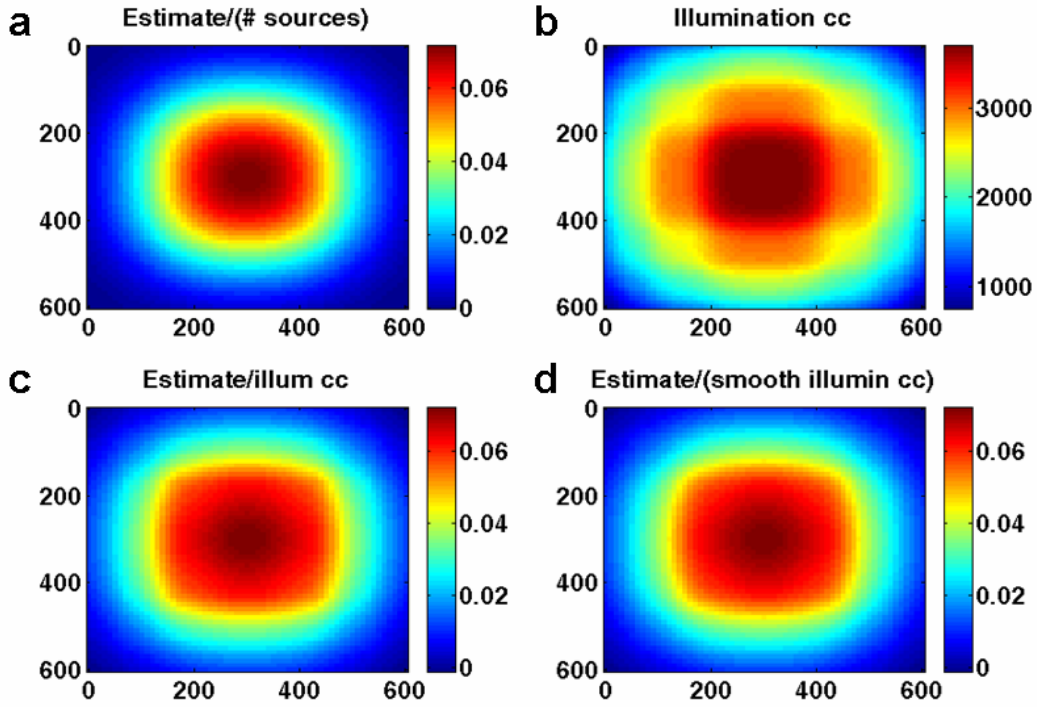
Figure 5. The PP algorithm results (similar to Figure 3) except that the I_{cc} illumination estimates (equation (22)) were used.
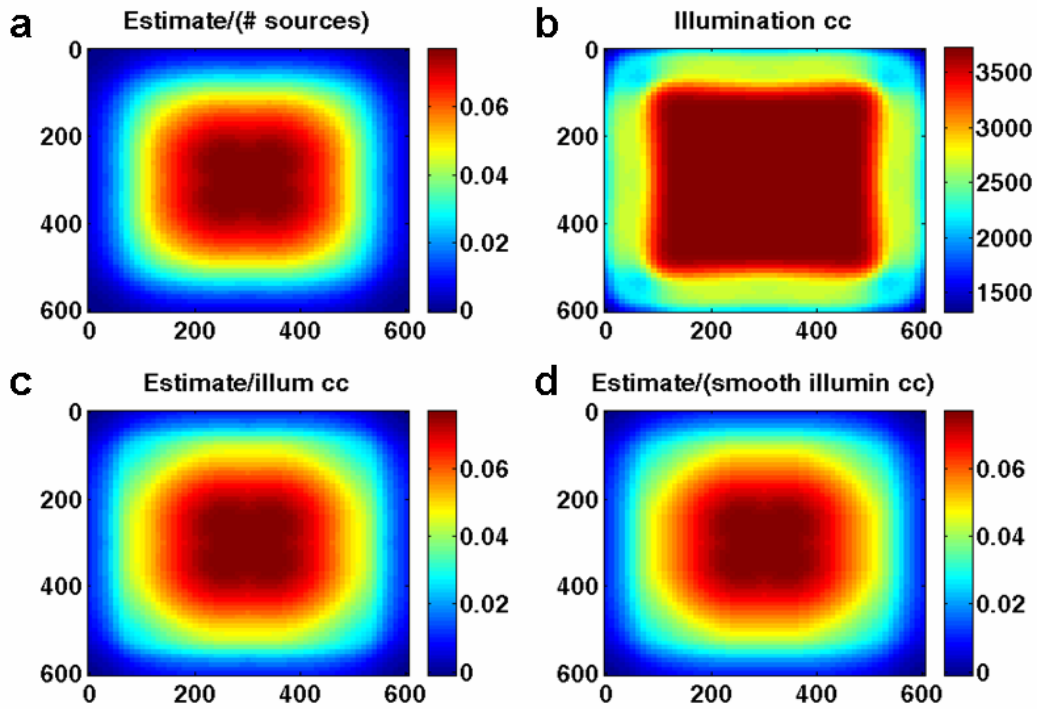
Figure 6. PS algorithm results (similar to Figure 4) except that the I_{cc} illumination estimates (equation (22)) were used.

At this point, there are a number of directions for possible exploration and, given constraints on time and space, only a few can be explored. Of interest would be

- the effects of random noise and surface noise. Different noise levels and noise spectra (for coherent noise) are of interest.

- the performance of the source-reduced and source-receiver reduced geometries.

- the variation of footprint effects for different depth/aperture ratios.

- the efficacy of further reductions in source effort.

- non-orthogonal line geometries.

No doubt the interested reader can add to this list. However, before digressing on any of these points, it is instructive to take a closer look at the details of imaging just four select sources. Figure 7 shows the location of the four sources to be examined, of course, by symmetry these four sources actually represent thirteen source locations in the survey aperture. Figure 8 shows PP data frequencies at 10 Hz as modeled at the surface using equation (14)). There was no noise of any kind in the simulation shown in Figures 8-18 and the full receiver geometry was used. Except for a bulk scale factor provide by the source shape function, $s(\omega)$, all frequencies will look identical at the surface. Figures 9 and 10 show 10 Hz. and 60 Hz. respectively after extrapolation to the reflector depth. The extrapolation has the effect of focusing the data in a zone about the specular reflection points. It might be expected that this would correspond to the expected S-R midpoints, that is the classical fold, but the grey boxes on each figure show that the correspondence is only approximate. Since ray theory is a high frequency theory, it is reassuring that the correspondence seems better at 60Hz than at 10. Figure 11 shows the forward modeled source at 10 Hz as evaluated at the reflector depth. This is an example of $D_j(x, y, z = 500, \omega)$ as required in equation (2). In Figures 12 and 13 are the reflectivity estimates calculated at 10 Hz and 60 Hz. Again the grey boxes show the limit of conventional fold. While this simulation is actually done for the 10-60 Hz band, Figure 14 is inserted to show that at 250 Hz, the estimate is almost entirely within the conventional fold box.

Figure 15 shows the final broadband reflectivity estimates formed by stacking together the estimate for each frequency between 10 and 60 Hz. In addition to having considerable power outside the classical fold box, the estimate has a particular geometric shape that is roughly an octagon. The illumination estimate $I_{r;j}$ corresponding to equation (20) is shown in Figures 16 and 17 while 18 and 19 document the illumination estimate $I_{cc;j}$ of equation (22). The crosscorrelation estimate seems surrounded by problematic rings that could lead to later difficulties. Since both illumination estimates are entirely positive, they will not have the same noise reduction ability as the direct stack of the broad band reflectivity estimates (i.e. the migrated shot records).
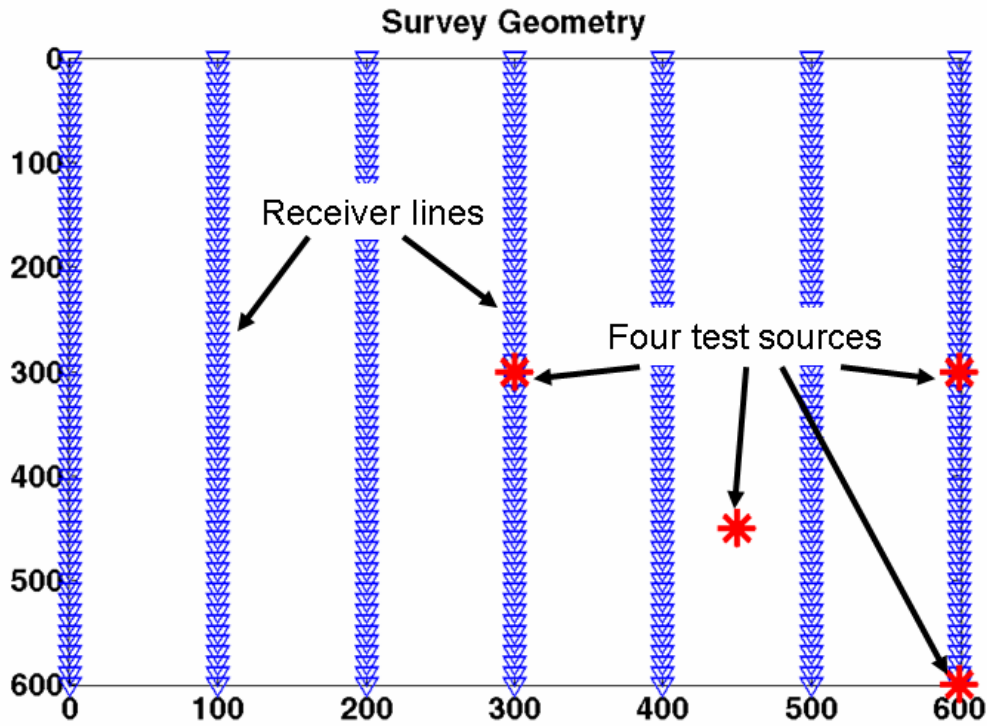
Figure 7. The locations of four test sources are shown.
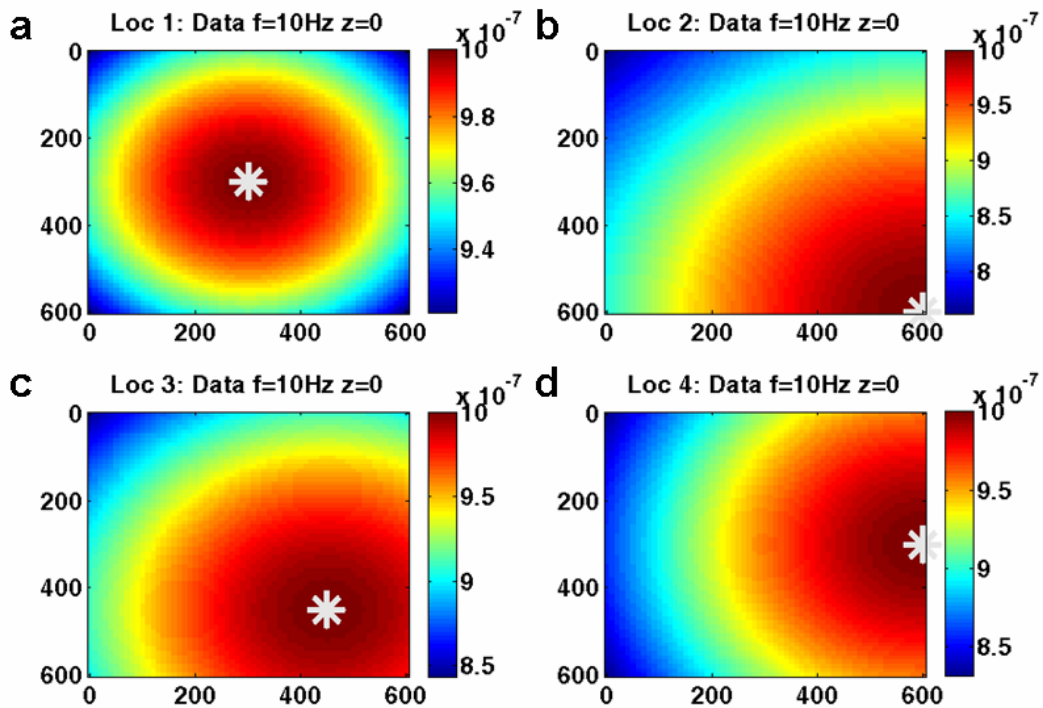
Figure 8: For the source locations of Figure 7, the magnitude of the forward modeled data at 10Hz is shown. All other frequencies will look the same (see equation (14)). The source locations are denoted by white stars.
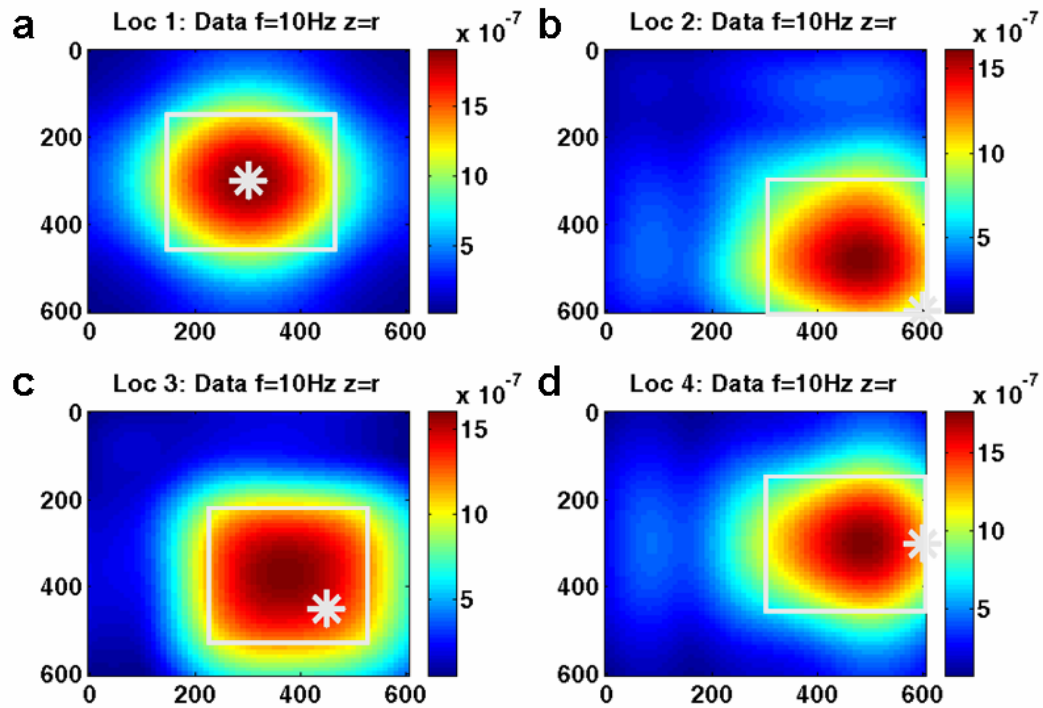
Figure 9. The data of Figure 8 after downward extrapolation to the reflector. This is $U_j(x, y, z = 500, \omega = 2\pi 10)$ in equation (2). The grey boxes indicate the extent of the classical fold as determined by the source-receiver midpoints.
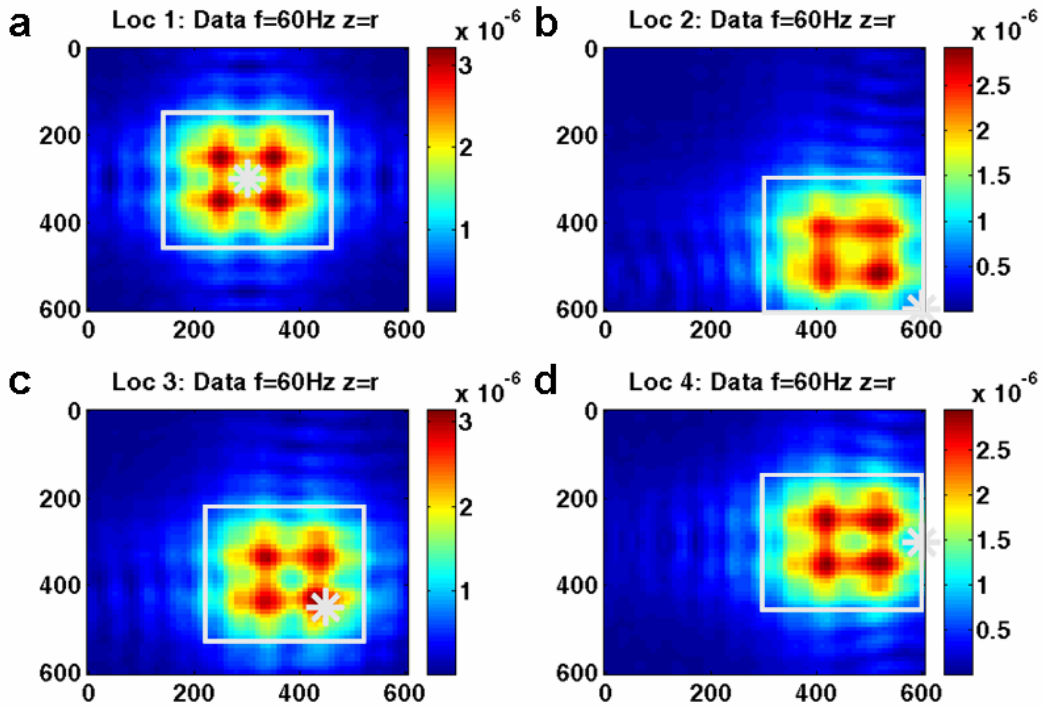
Figure 10. The data at 60 Hz. after downward extrapolation to the reflector. This is $U_j(x, y, z = 500, \omega = 2\pi 60)$ in equation (2). The grey boxes indicate the extent of the classical fold as determined by the source-receiver midpoints.
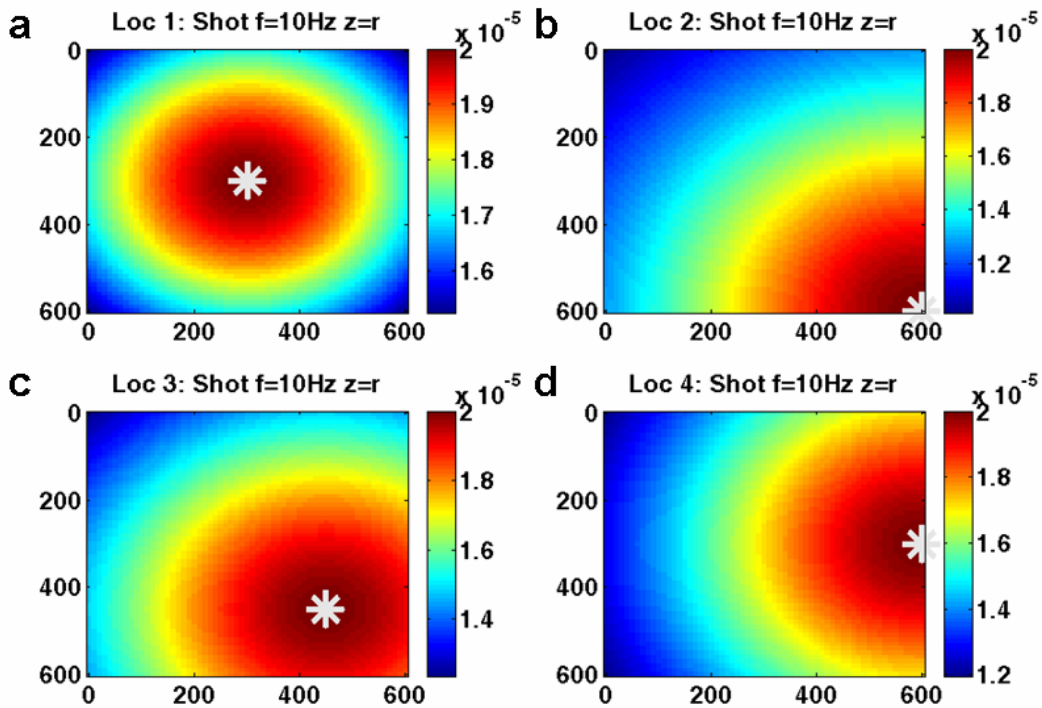
Figure 11 The source estimate (magnitude) at the reflector for 10 Hz. This is $D_j(x, y, z = 500, \omega = 2\pi 10)$ in equation (2). All other frequencies will look the same.

.
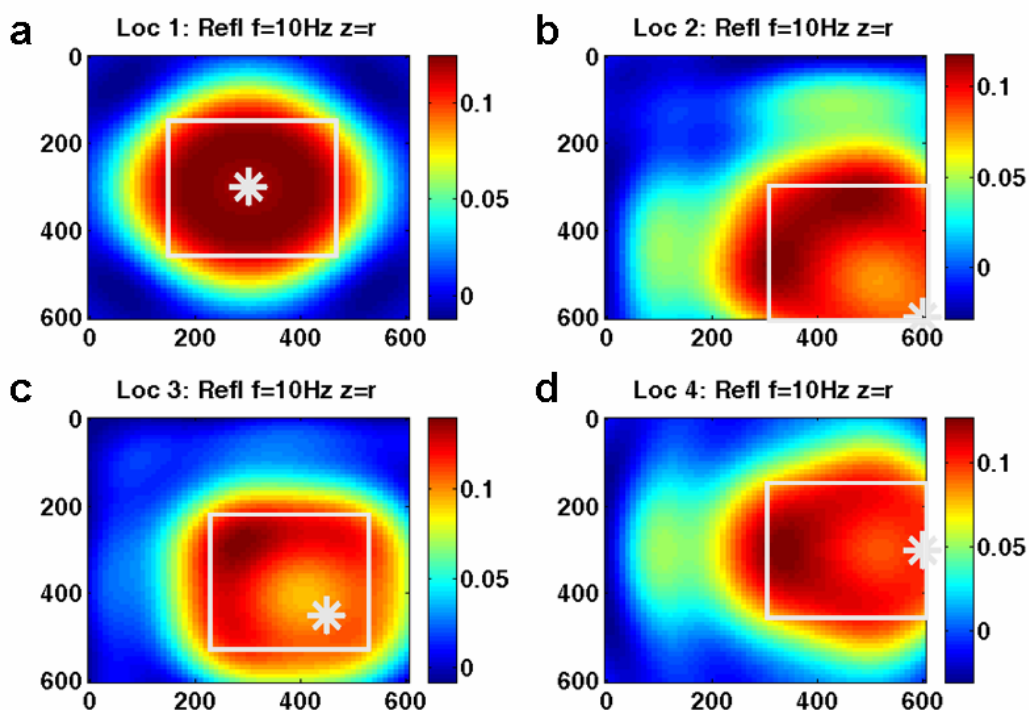
Figure 12. The reflectivity estimate for 10 Hz (see equation (2). The grey boxes indicate the extent of the classical fold as determined by the source-receiver midpoints.
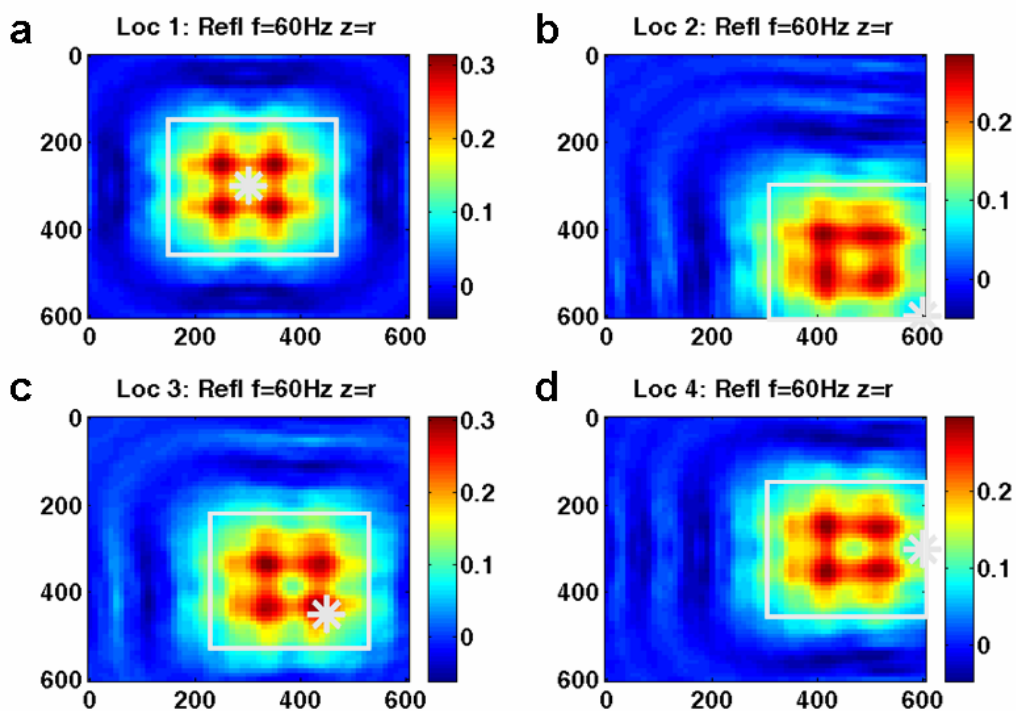
Figure 13. The reflectivity estimate for 60 Hz (see equation (2). The grey boxes indicate the extent of the classical fold as determined by the source-receiver midpoints.
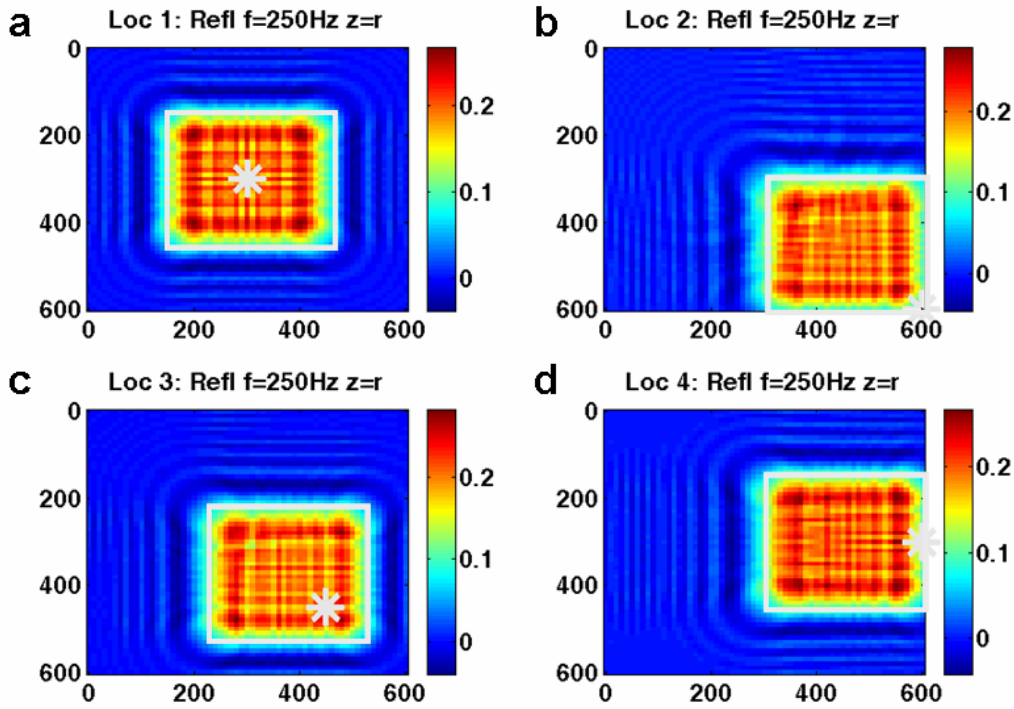
Figure 14. The reflectivity estimate for 250 Hz (see equation (2). Note that the estimate is largely confined to the grey boxes that indicate the extent of the classical fold.
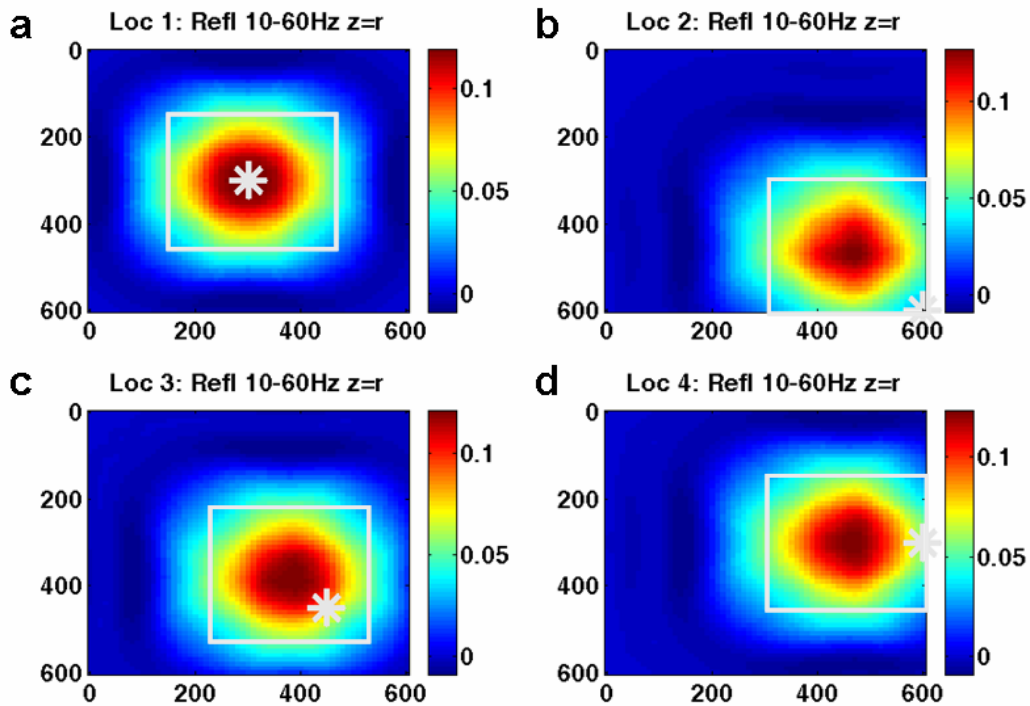
Figure 15. The broadband reflectivity estimate for 10-60 Hz. This is the stack of individual frequency estimates like those of Figures 12 and 13 for all frequencies between 10 and 60 Hz. The grey boxes indicate the extent of the classical fold as determined by the source-receiver midpoints.
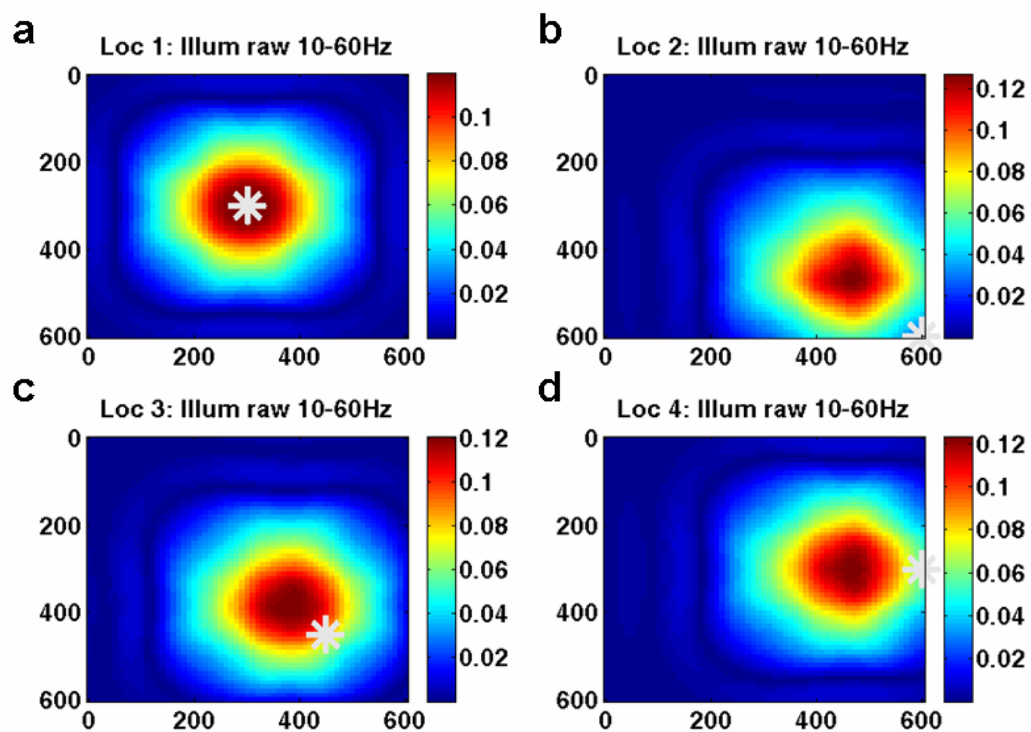
Figure 16. The raw illumination (before thresholding) corresponding to I_r in equation (20). Effectively, this is I_r with the threshold $\mu = 0$.
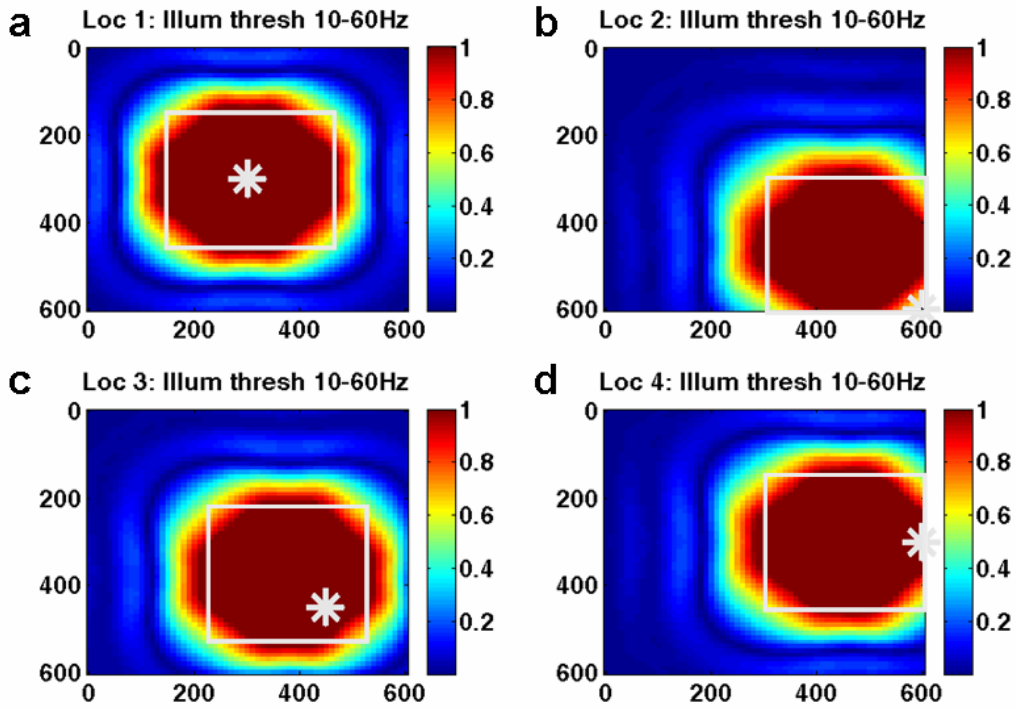
Figure 17. The result of applying the threshold $\mu = 0.4$ to the raw illumination of Figure 15. See equation (20) also. The grey boxes indicate the extent of the classical fold as determined by the source-receiver midpoints.
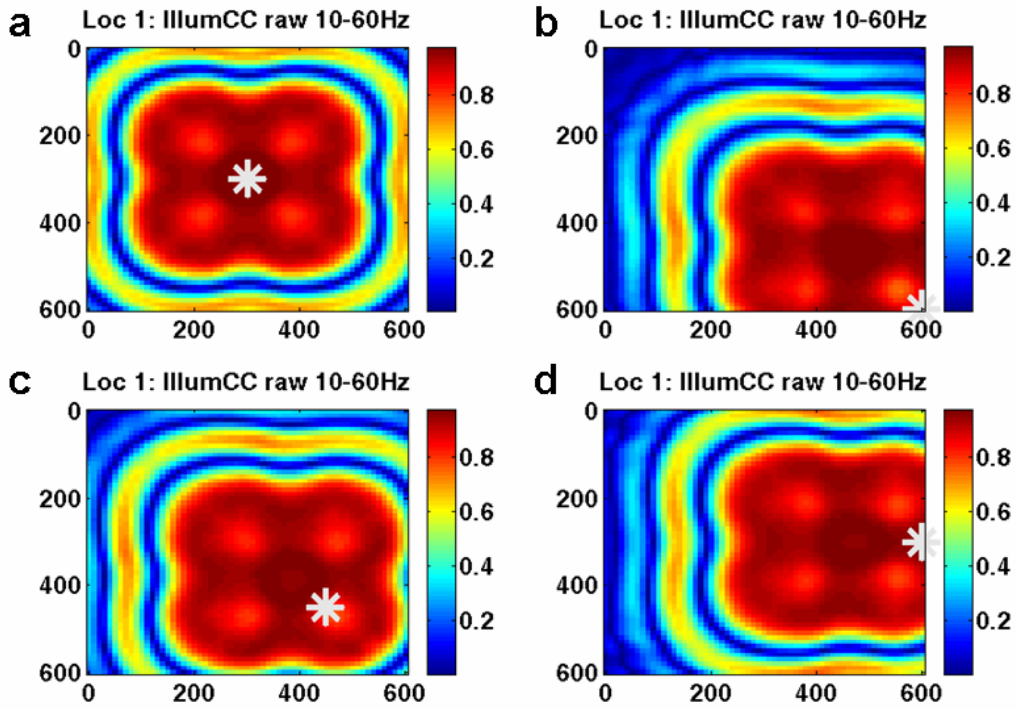
Figure 18. The raw illumination I_{cc} (equation (22) with $\nu = 0$).
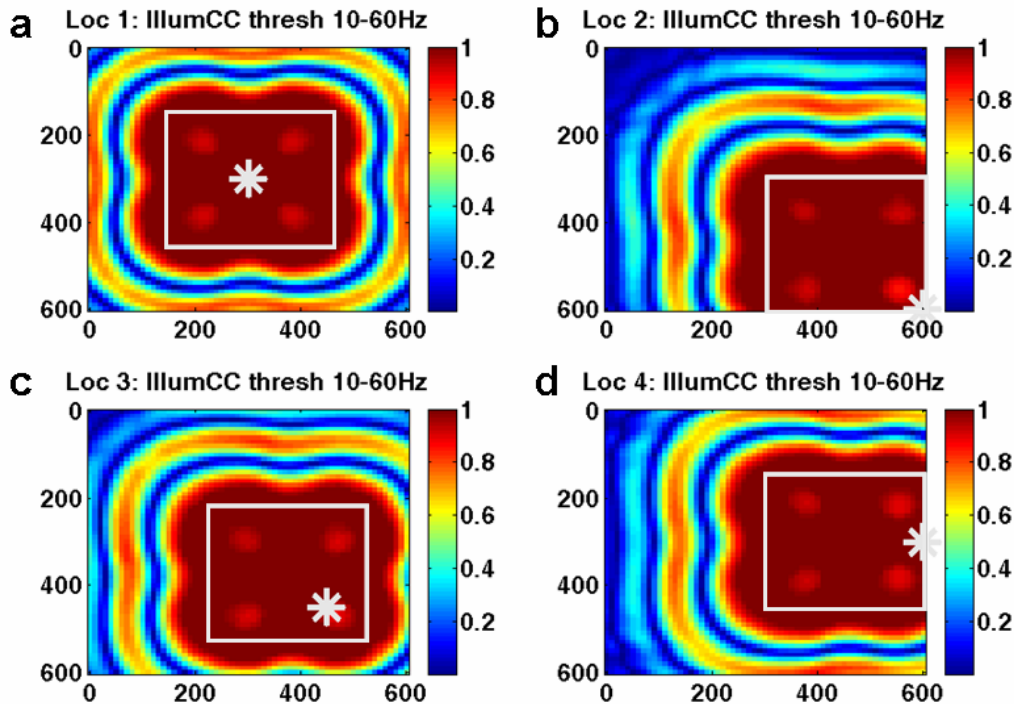
Figure 19. The illumination I_{cc} (equation (22)) with $\nu = .9$. The grey boxes indicate the extent of the classical fold as determined by the source-receiver midpoints. The grey boxes indicate the extent of the classical fold as determined by the source-receiver midpoints.

Effects of geometry reduction

Figure 20 shows a PP experiment using the source-reduced geometry (see Figure 1) and the I_r illumination estimate. In comparison to Figure 3, it appears that the estimate is hardly affected by the source reduction, which is not surprising given that there is no noise at this point. In Figure 21 is the noise-free estimate from the source-receiver reduced geometry in the PP case and not significant vertical striping is seen. The illumination compensation seems to reduce the striping artifact but it is still present even after compensation.

As Figures 22 and 23 show, the situation is similar with the PS case. Since the simulation is done with the same frequency bandwidth as the PP case (10-60 Hz), the slower S-wave velocity (1500 m/s instead of 3000 m/s) means that the wavenumber spectral width is twice as wide. This may be somewhat unrealistic since apparent PS bandwidths in actual experiments are usually considerably less than the corresponding PP. Nevertheless, the results are instructive. While the source-reduced geometry performs reasonably well, the source-receiver reduced geometry has a somewhat more significant vertical striping artifact than in the PP case.
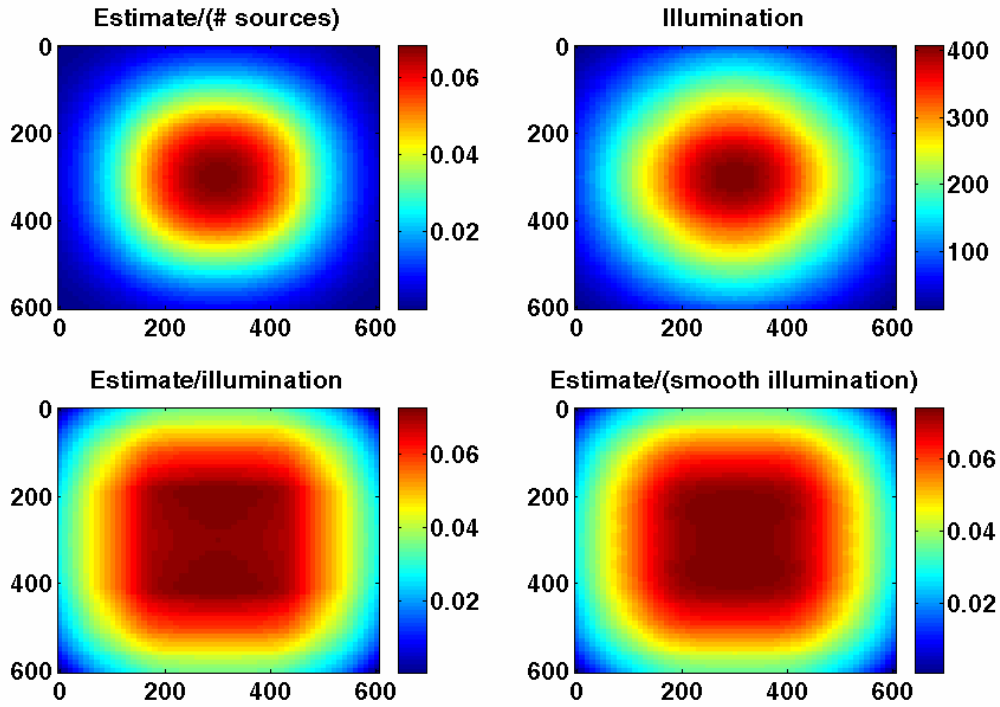
Figure 20. A PP experiment, similar in all ways to Figure 3 except that the source-reduced geometry is used.
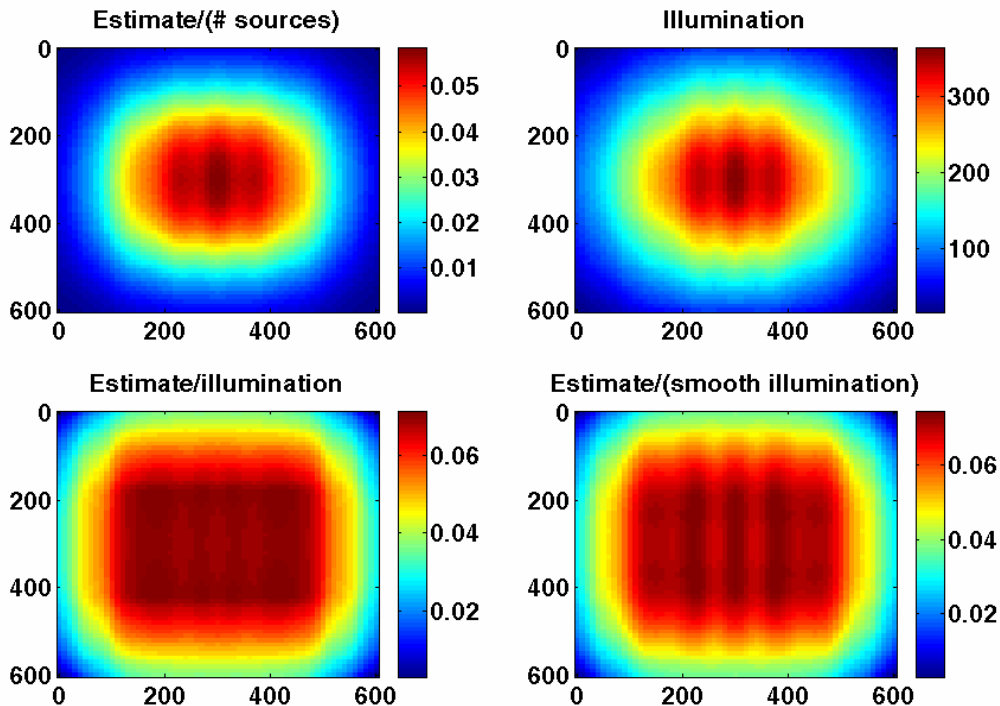
Figure 21. A PP experiment, similar in all ways to Figure 20 except that the source-receiver reduced geometry was used.
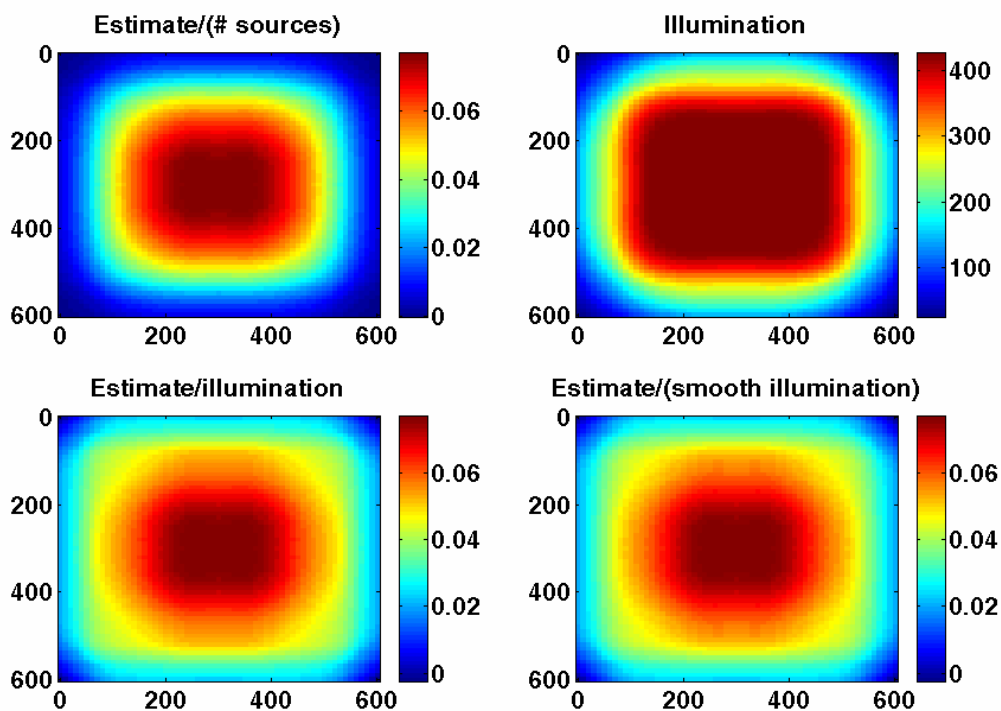
Figure 22. A PS experiment, similar in all ways to Figure 4 except that the source-reduced geometry was used.
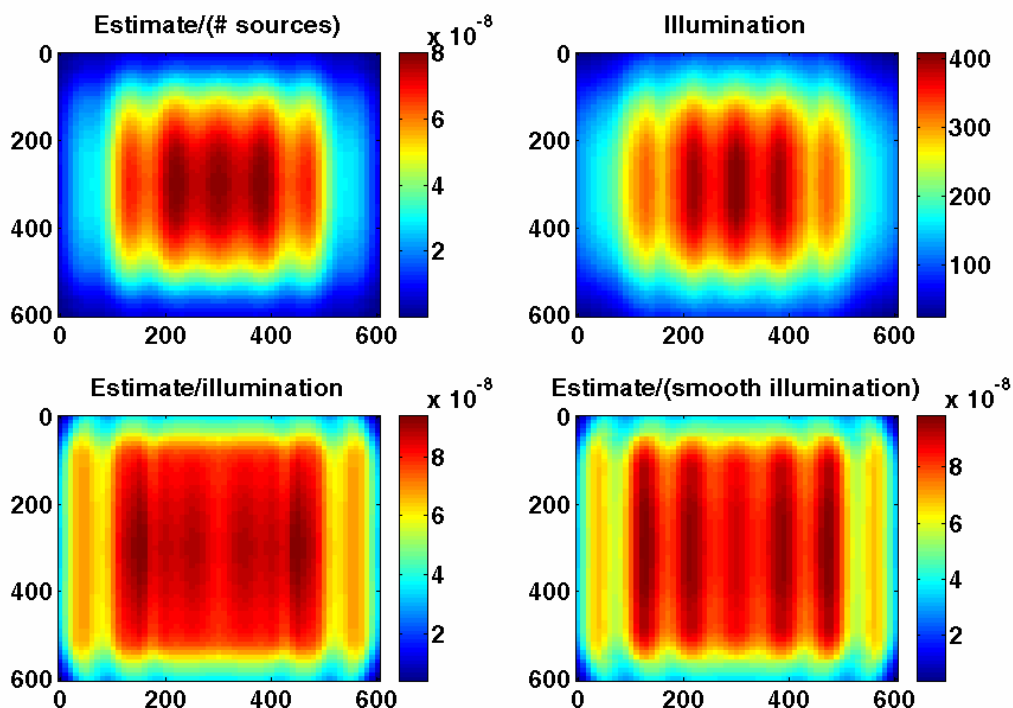
Figure 23. A PS experiment, similar in all ways to Figure 22 except that the source-receiver reduced geometry was used.

As an interesting aside, Figure 24 shows the result of a PP experiment using the source-receiver reduced geometry but with the twist that the source lines are parallel and on top of the receiver lines. This result almost seems better than the orthogonal geometry and this is not presently understood. Note that the code released with this paper is not immediately capable of producing this result and that a special purpose code was used.
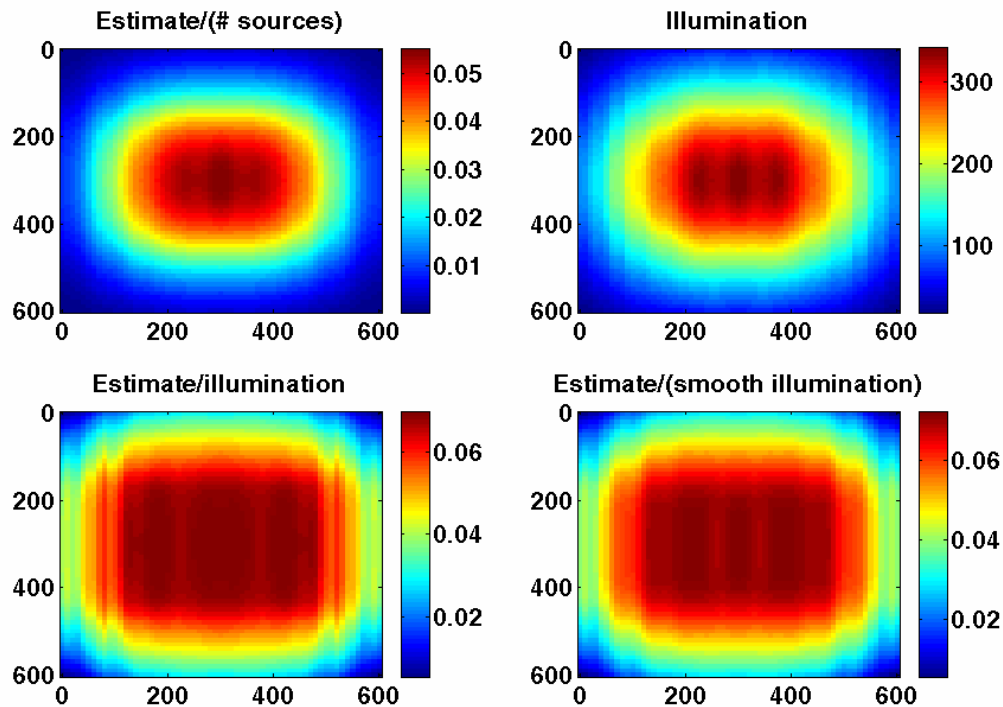
Figure 24. A PP experiment using source-receiver reduced geometry, and therefore similar to Figure 21, except that the source lines are parallel to, and on top of, the receiver lines.

Effects of random noise

The footprint codes include the ability to include additive, Gaussian distributed, zero mean, random noise. The noise level is specified via the parameter called "N2S" meaning the noise-to-signal level. This is preferred to signal-to-noise level since the value N2S=0 has the simple meaning of no noise. The parameter N2S prescribes the ratio of the noise power to the signal power at the dominant frequency of the simulation. Since the spectral shape function, $s(\omega)$ in equation (14), is a raised cosine extending from $\omega_{\min}$ to $\omega_{\max}$, then the dominant frequency is $\omega_{dom} = (\omega_{\max} + \omega_{\min})/2$. Though the noise power is specified at the dominant frequency it has the same power at all frequencies. Figure 25 shows the effect of different N2S settings.

Figure 26 shows the results of a PP experiment using the source-receiver reduced geometry with N2S=1, and the I_r illumination calculation. Figure 27 is similar except that the I_{cc} illumination was used. The inclusion of such a high level of random noise has seriously degraded the estimations. The apparent symmetry in the noise patterns is an artifact of the modeling process which only calculates sources explicitly in one

quadrant of the image and deduces the others by symmetry operations. While both of these results are severely degraded relative to Figure 21 for example, it is interesting to note how much smoother the I_{cc} estimate is than the I_r. Since the former is just a thresholded, normalized cross-correlation, it suggests that perhaps the crosscorrelation imaging condition (equation (3)) would give better results. Figure 28 shows a repeat of the calculation of Figure 26 using the crosscorrelation imaging condition and the results are indeed much better.
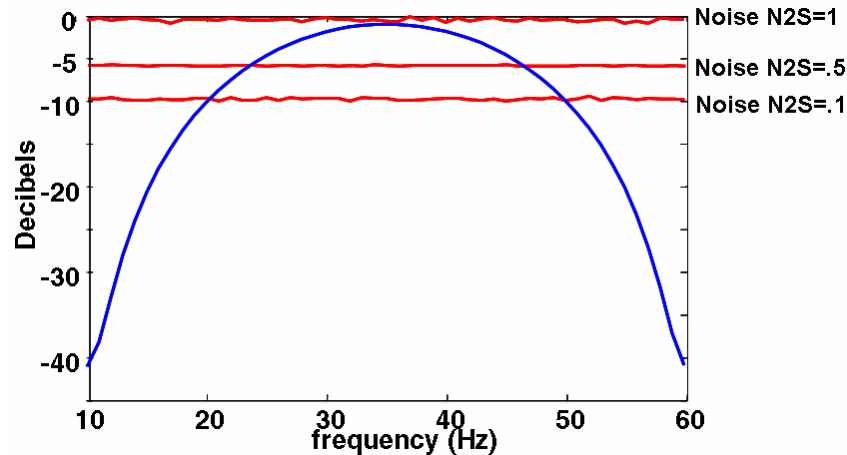
Figure 25. The blue curve shows the raised cosine $s(\omega)$ for the case $\omega_{\min} = 2\pi 10$ and $\omega_{\max} = 2\pi 60$. The various red curves show the noise levels created by the indicated values of the parameter N2S.

Now, returning to the deconvolution imaging condition, Figures 29 and 30 are intended to convey the additional noise reduction achieved by using the un-reduced receiver geometry. Figure 29 shows the result of a PP experiment using N2S=0.5 and the source-receiver reduced geometry. Figure 30 is similar except that the full receiver geometry was used. Clearly there is greater noise reduction in the second case. In fact, Figure 31 used the source-receiver reduced geometry but with N2S=0.1 and the result is similar to Figure 30. Thus it appears that the inclusion of all receivers is similar to lowering the N2S level from 0.5 to 0.1. This effect is illustrated on the four individual source records (Figure 7) in the sequence of Figures 32, 33, and 34.
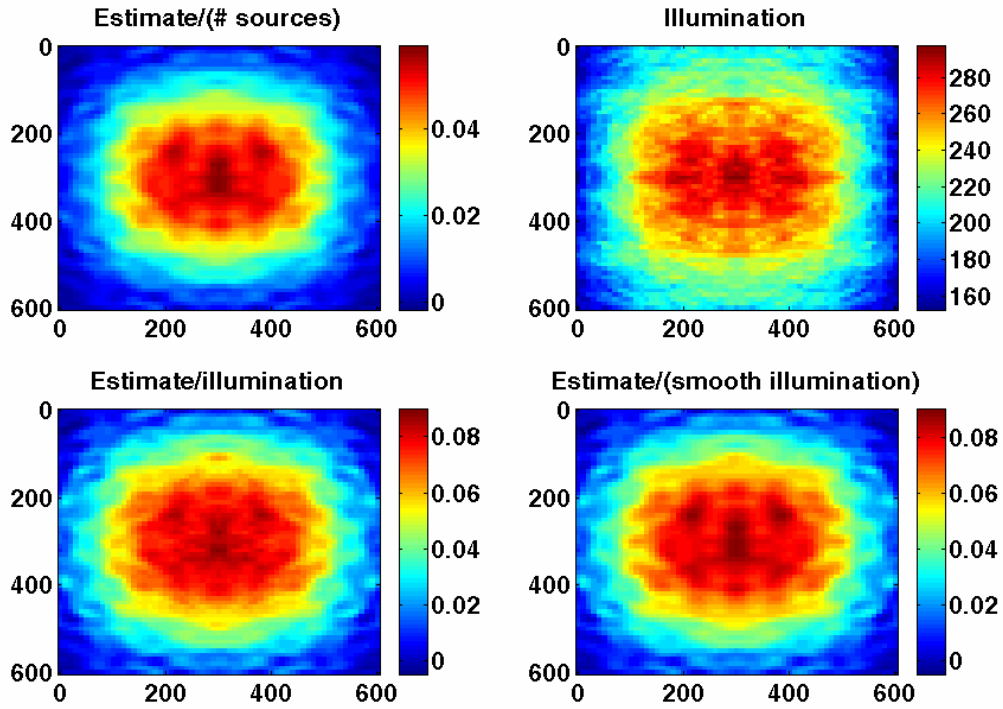
Figure 26. A PP experiment, using the source-receiver reduced geometry and therefore similar to Figure 21, with added random noise. The noise corresponds to N2S=1. The I_r illumination calculation was used.
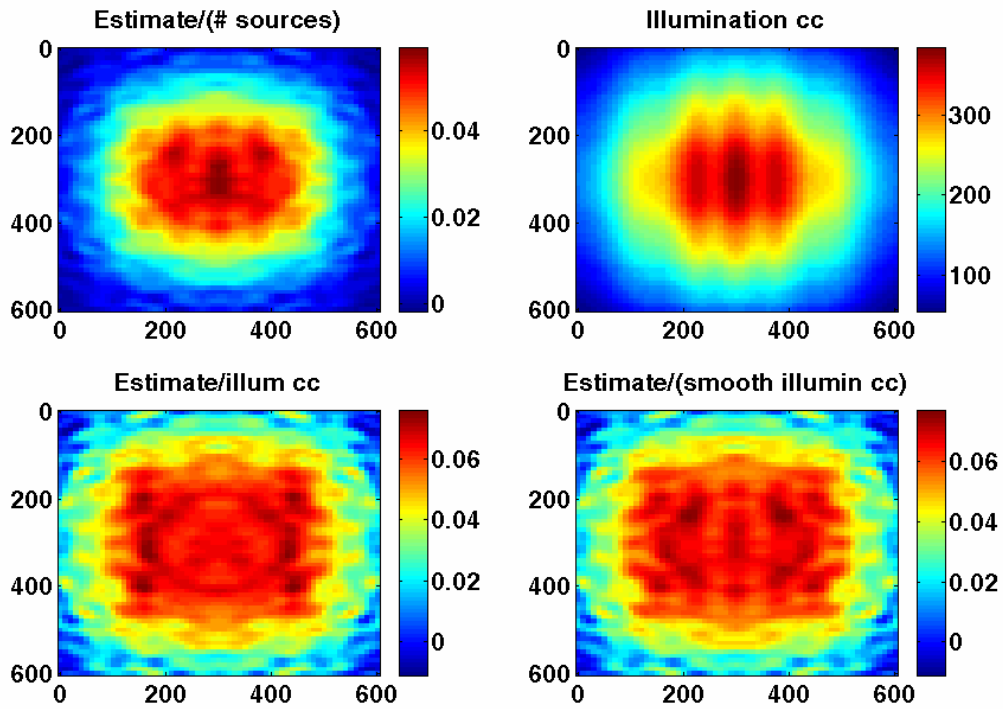
Figure 27. Similar to Figure 26 except that the I_{cc} illumination calculation was used.
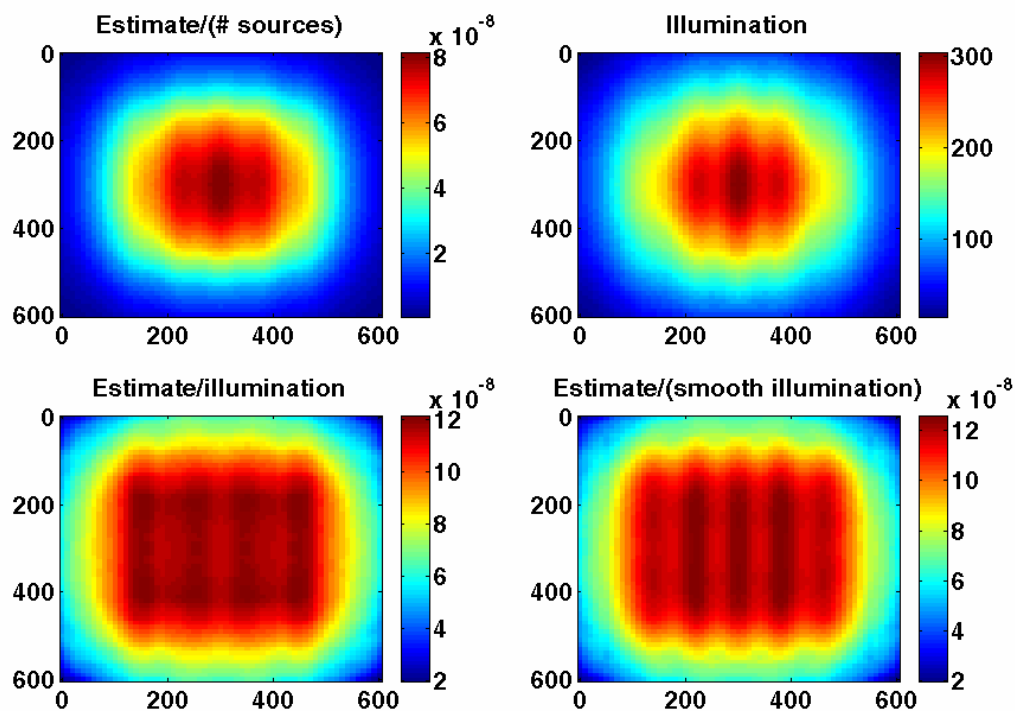
Figure 28. Similar to Figure 26 except that the crosscorrelation imaging condition was used.
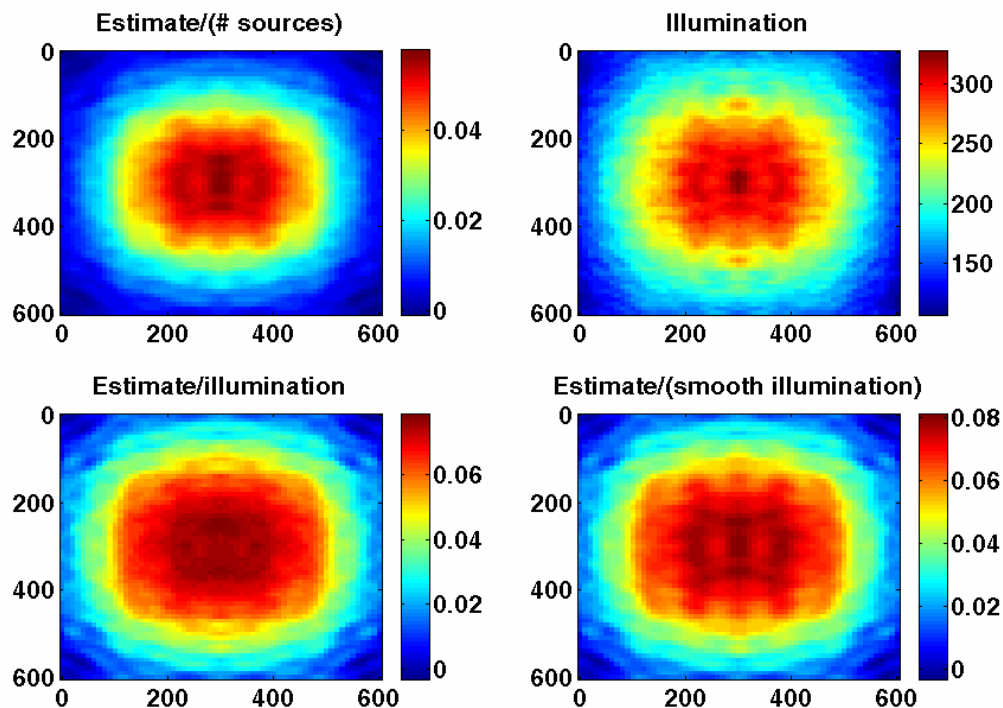
Figure 29. A PP experiment using source-receiver reduced geometry for N2S=0.5.
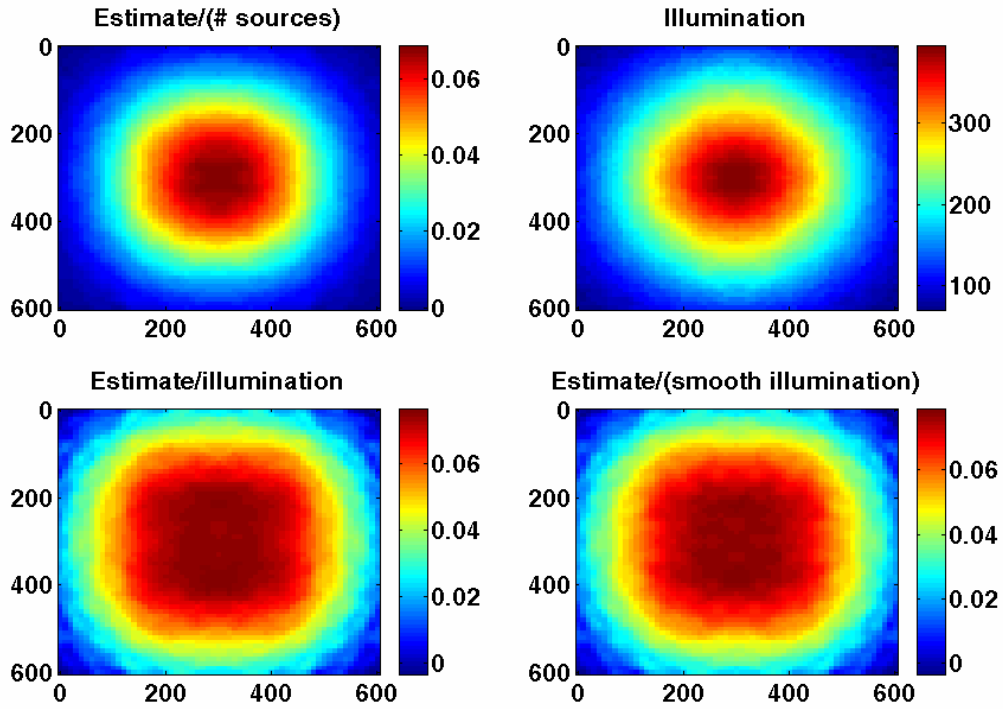
Figure 30. Similar to Figure 29 except that the source-reduced geometry was used. That is, the full receiver geometry contributed to the noise reduction.
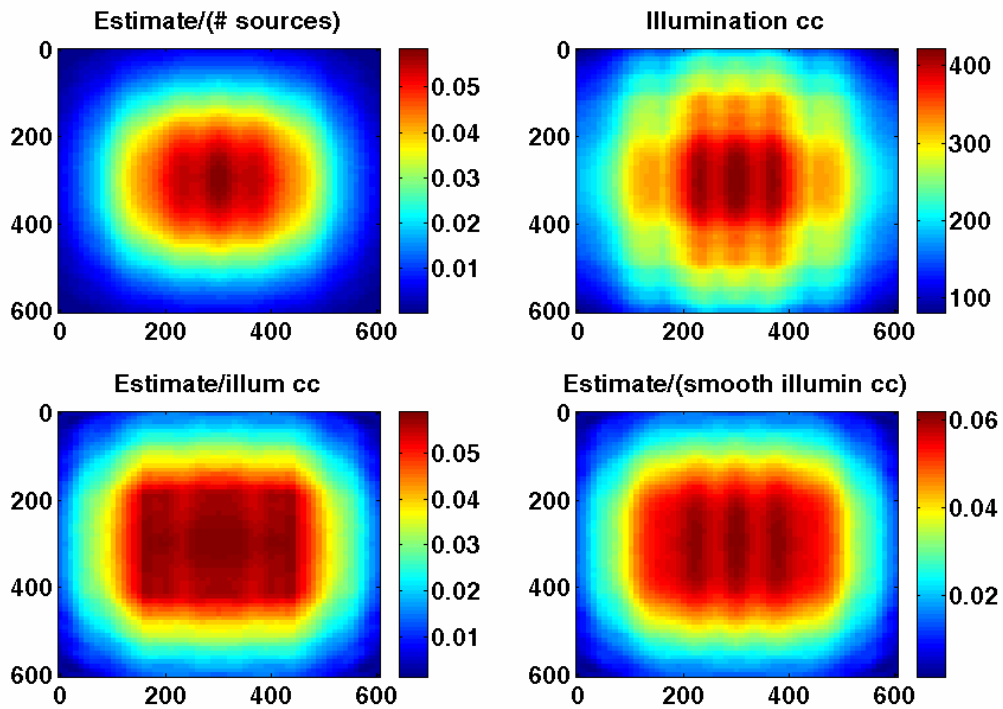
Figure 31. Similar to Figure 29 except that the noise level is given by N2S=0.1 .
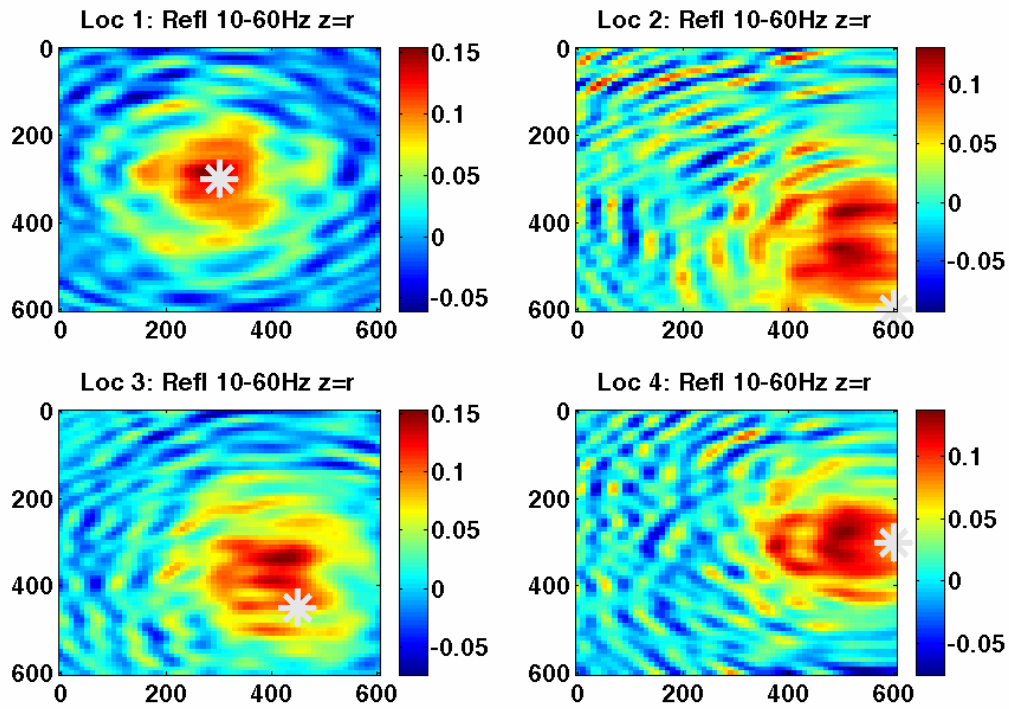
Figure 32. The broadband reflectivity estimates for the four sources of Figure 7 simulated with N2S=0.5 and the receiver reduced geometry. Compare with Figure 15.
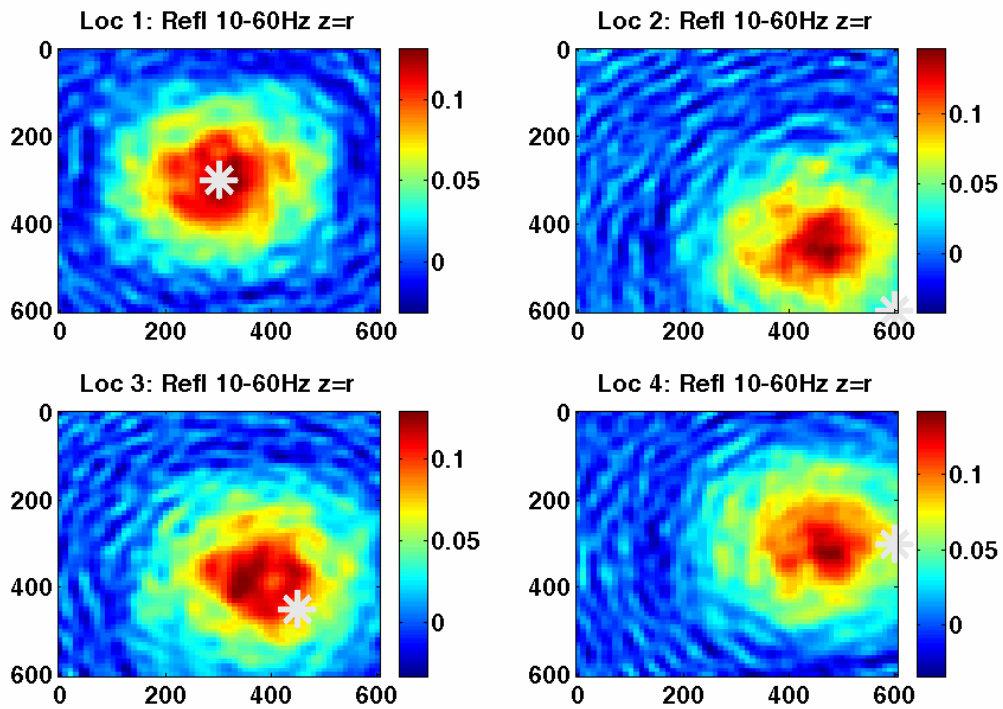
Figure 33. Similar to Figure 32 except that the full receiver geometry was used.
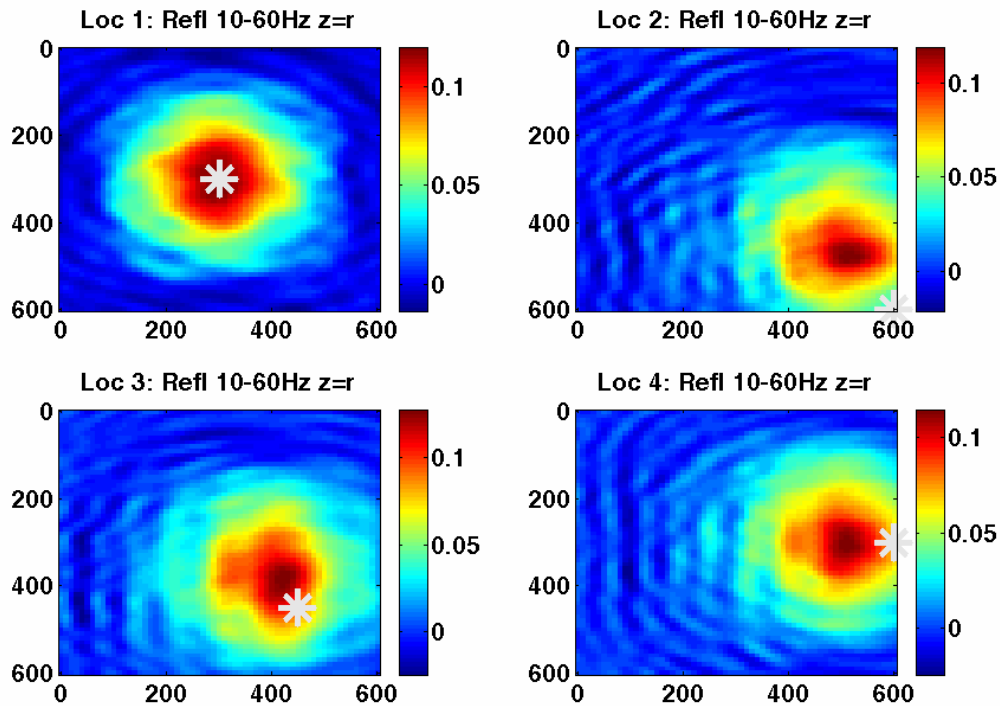
Figure 34. Similar to Figure 32 (i.e. using the receiver reduced geometry) except that N2S=0.1. Compare also with 33.

Effects of surface waves

Surface waves are modeled in the *footprint* codes as linear events in time with a characteristic velocity, spectral shape function, and strength (velocity dispersion is not modeled). In the frequency domain, this becomes equation (17). The codes require the specification of the ratio of the strength of the surface waves to the reflection data at a reference offset and reference frequency, called $a_{relsurf}$. This allows the calculation of the a_{surf} scalar in equation (17) as

$$a_{surf} = \frac{ca_{relsurf}\, s\left(\omega_{ref}\right)\sqrt{h_{ref}}}{s_{surf}\left(\omega_{ref}\right)\sqrt{4z_0^2 + h_{ref}^2}}. \tag{25}$$

Figure 35 shows a PP experiment similar to Figure 20 except that surface waves are now present with a strength of $a_{relsurf} = 10$. There is very little effect of the surface waves in this case. Figure 36 is similar except that the geometry is now the source-receiver reduced case. In Figure 37, the source-receiver reduced geometry is still present but the surface wave strength has increased to $a_{relsurf} = 50$. It is apparent that surfaces waves are affecting the footprint though much of the effect is confined to the illumination estimation.
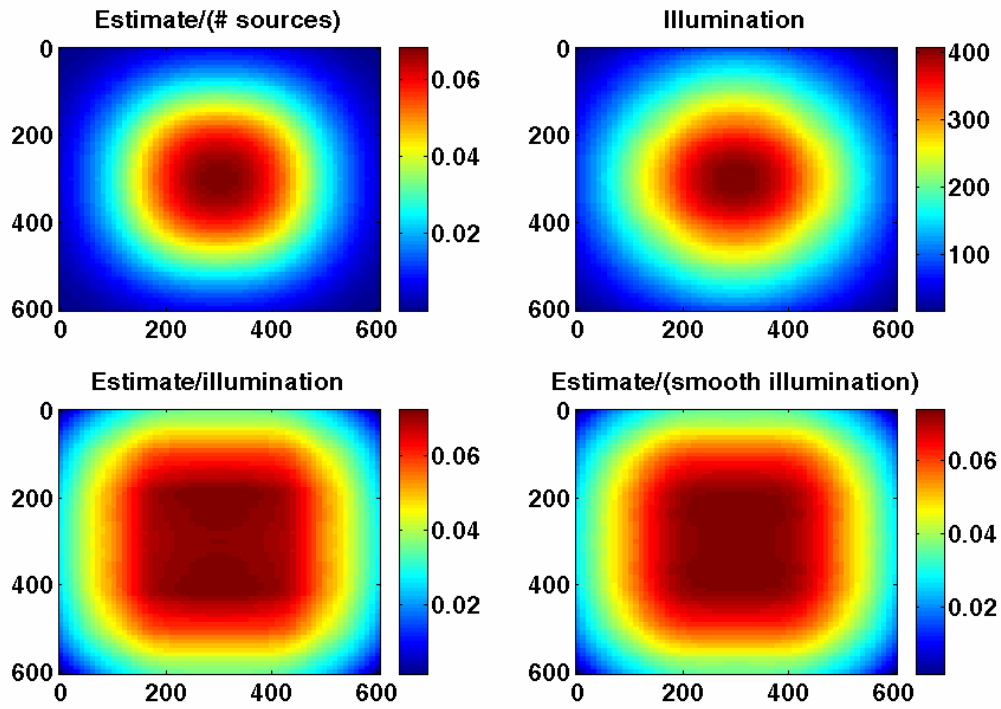
Figure 35. A PP experiment using the source-reduced geometry and a surface wave factor $a_{relsurf} = 10$. Compare with Figure 20.
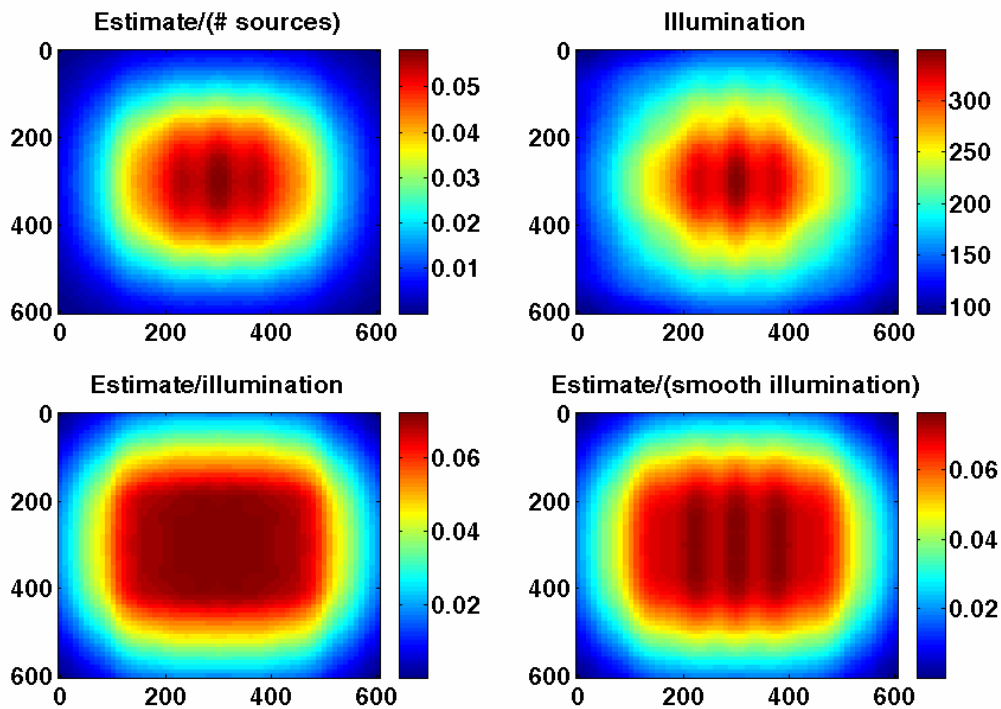
Figure 36. Similar to Figure 35 except that the source-receiver reduced geometry was used.
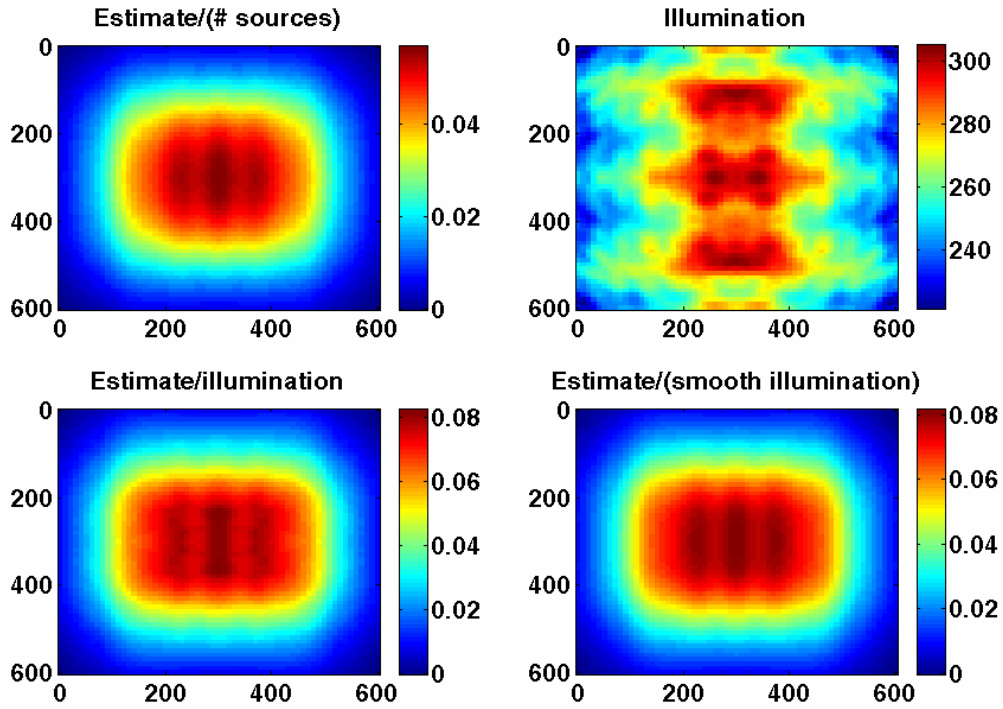
Figure 37. Similar to Figure 36 except the surface waves are stronger with $a_{relsurf} = 50$.
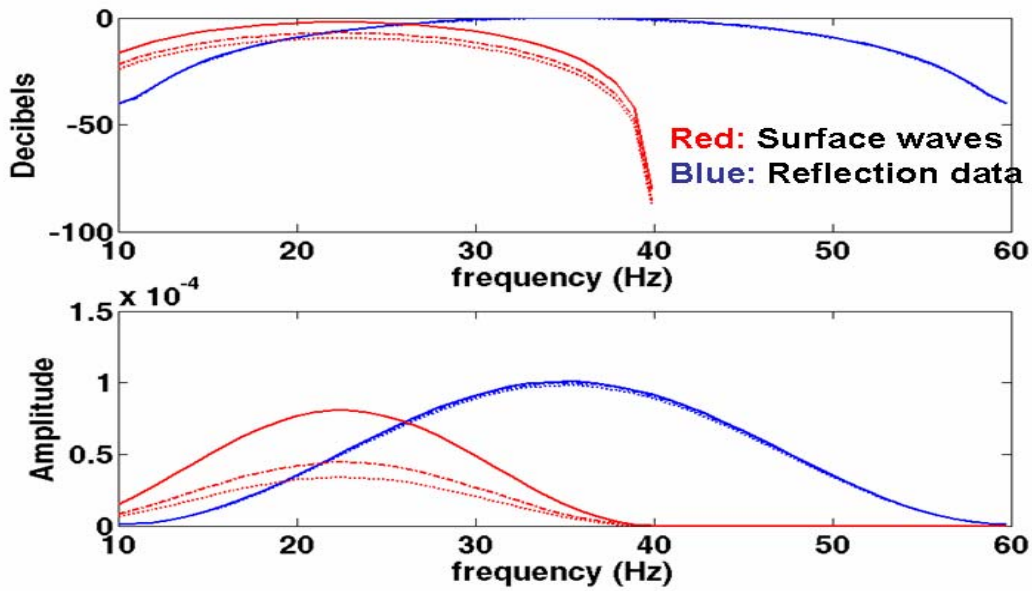

Figure 38. The surface wave and reflection data spectra corresponding to $a_{relsurf} = 1$. Red curves are surface wave spectra and blue curves are reflection data. Different curves correspond to near middle and far offsets.
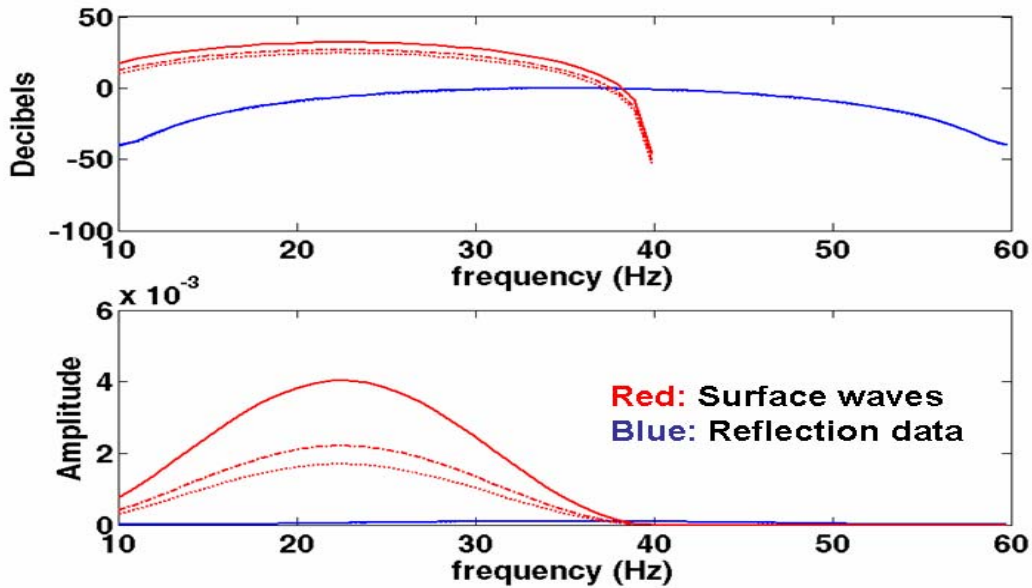
Figure 39. Similar to Figure 37 except that $a_{relsurf} = 50$.

Figures 38 and 39 are included to illustrate the flexibility in the *footprint* codes to model surface waves and reflection data of differing strengths and bandwidths. While this gives a great deal of modeling flexibility, it is difficult to summarize the effects in a short paper such as this.

In Figures 40-45, we return to examination of the four test sources of Figure 7. These figures track the broadband reflectivity estimate through a sequence of increasingly problematic surface waves. In Figure 40, there are no surface waves and the full receiver geometry is used. In Figure 41, there are still no surface waves but now the reduced receiver geometry is used. Then, in Figures 42-45 surface waves are included in ever increasing strength. In the final instance, with $a_{relsurf} = 100$ there is clearly a very big effect.

Finally, in Figures 46-51 the effect of the surface wave inclusion is shown on individual frequencies and at intermediate stages in the calculation for the case $a_{relsurf} = 10$. Studying these figures indicates that the frequencies where surface waves are present are very strongly disrupted. The broadband reflectivity estimate is largely saved by the higher frequencies which are free of the surface waves. The greater the spectral overlap the worse the situation.
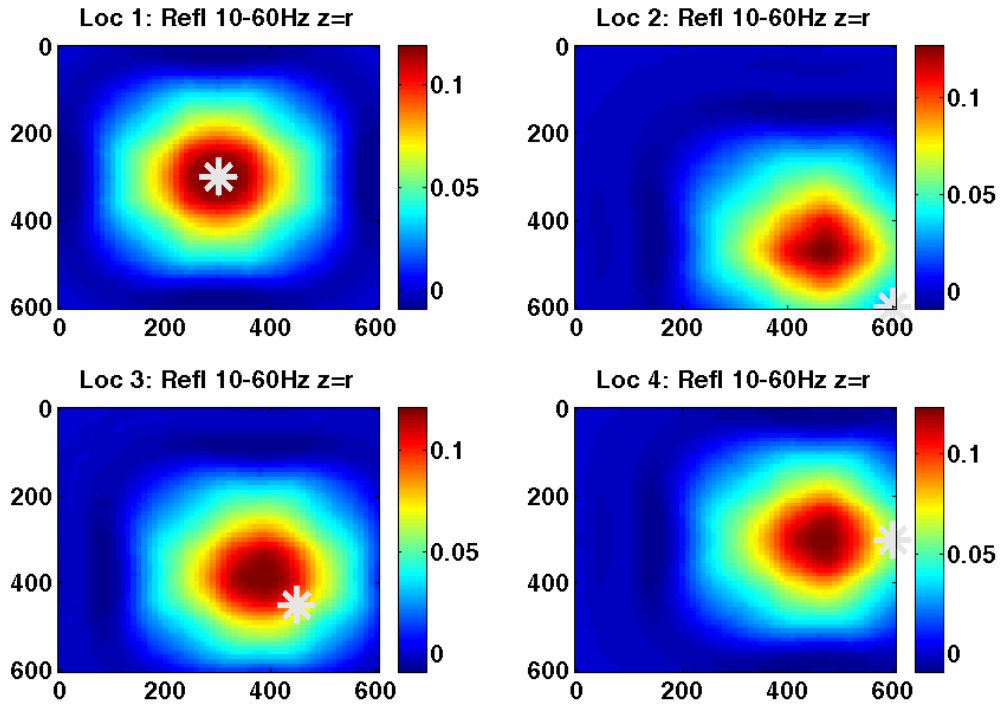
Figure 40. The broadband reflectivity estimate for the four test sources of Figure 7. No surface waves and the full receiver geometry was used.
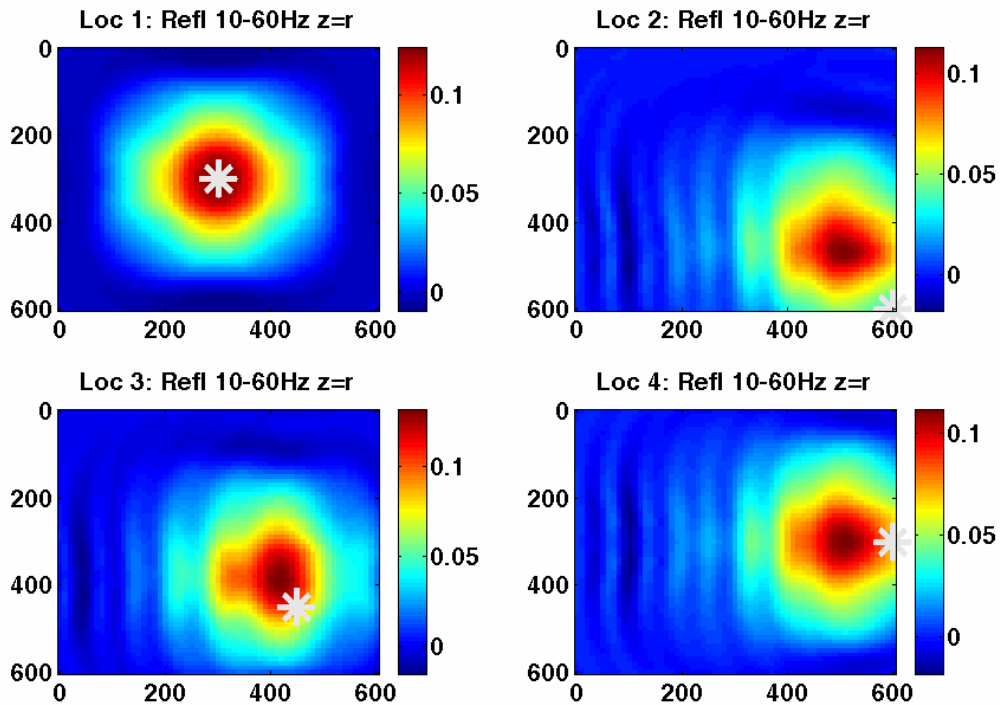

Figure 41. Similar to Figure 40 except that the receiver reduced geometry was used.
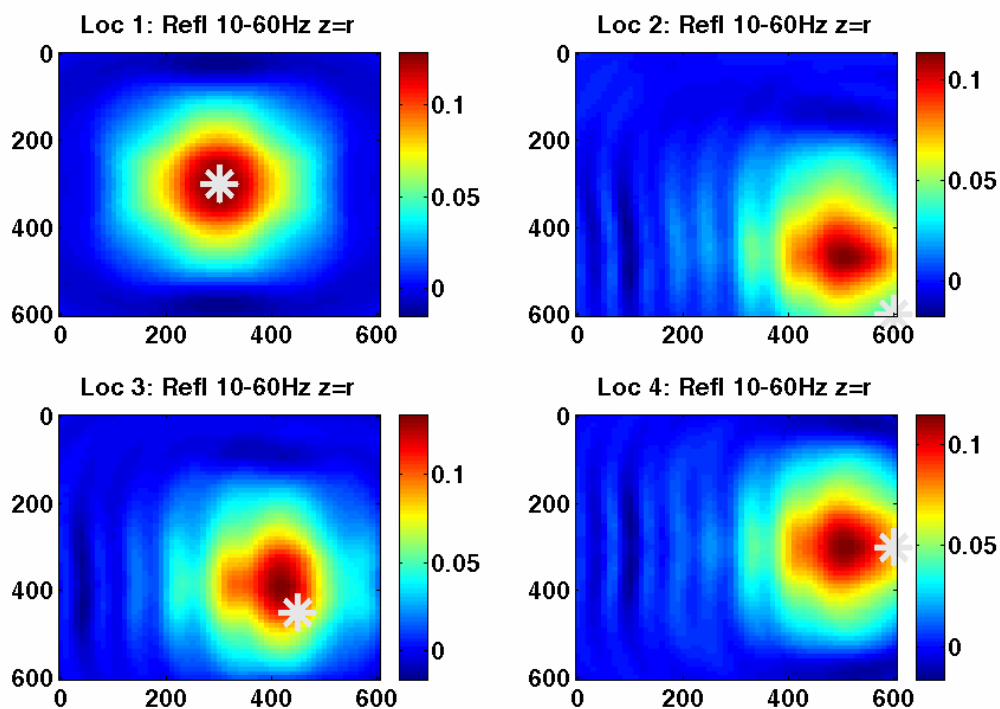
Figure 42.   Similar to Figure 41 except that surface waves are now present with strength $a_{relsurf} = 1$.
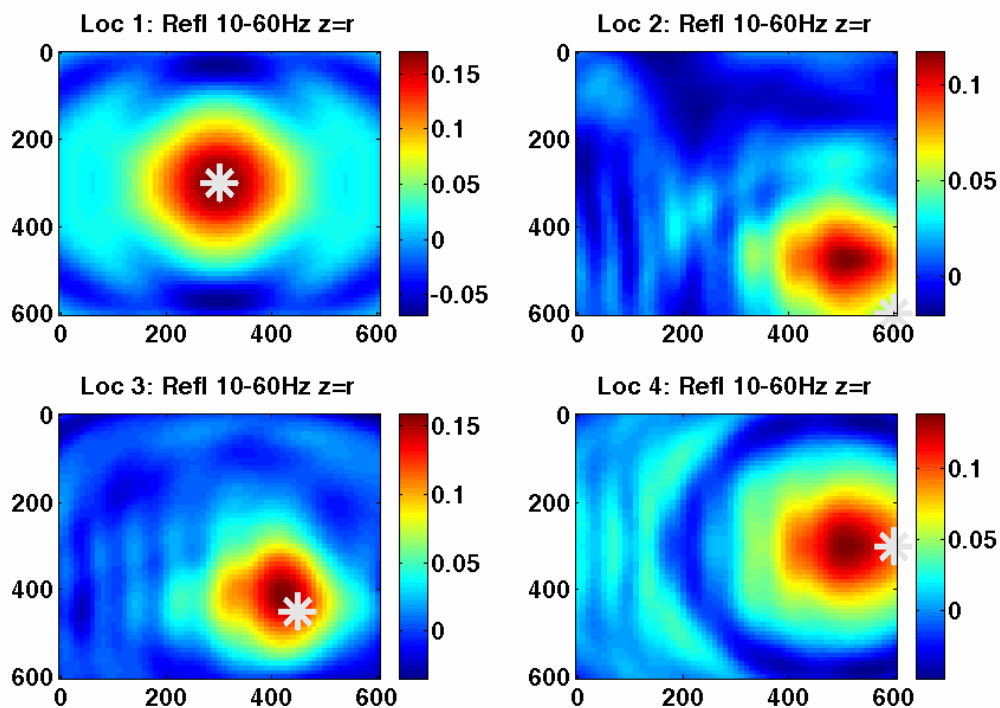

Figure 43.   Similar to Figure 42 except that surface wave strength has increased to $a_{relsurf} = 10$.
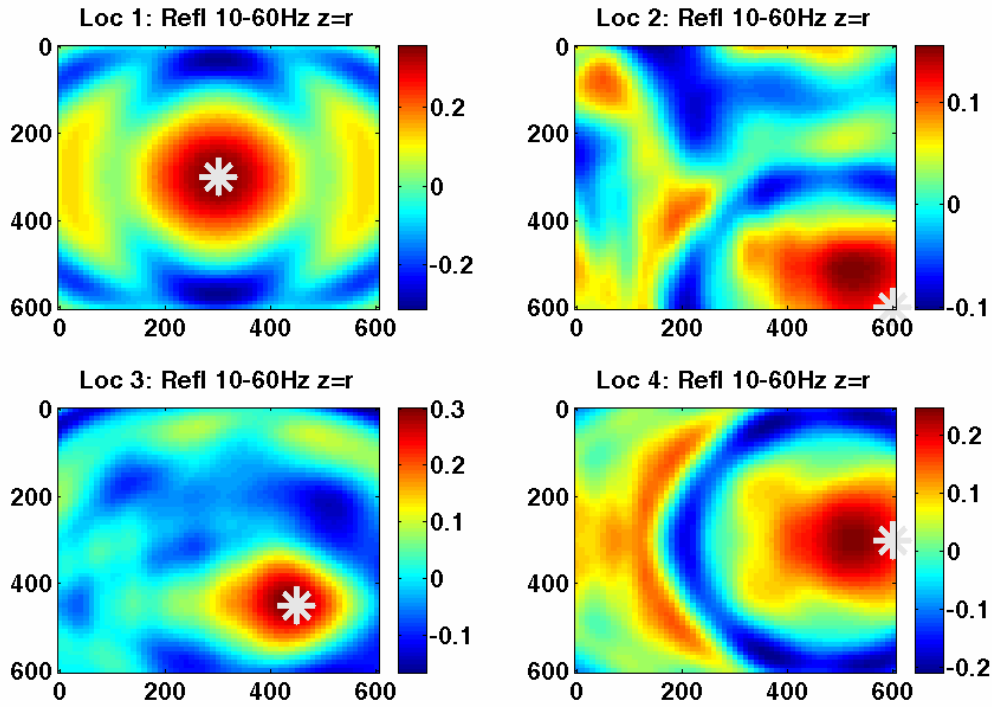
Figure 44. Similar to Figure 43 except that surface wave strength has now increased to $a_{relsurf} = 50$.
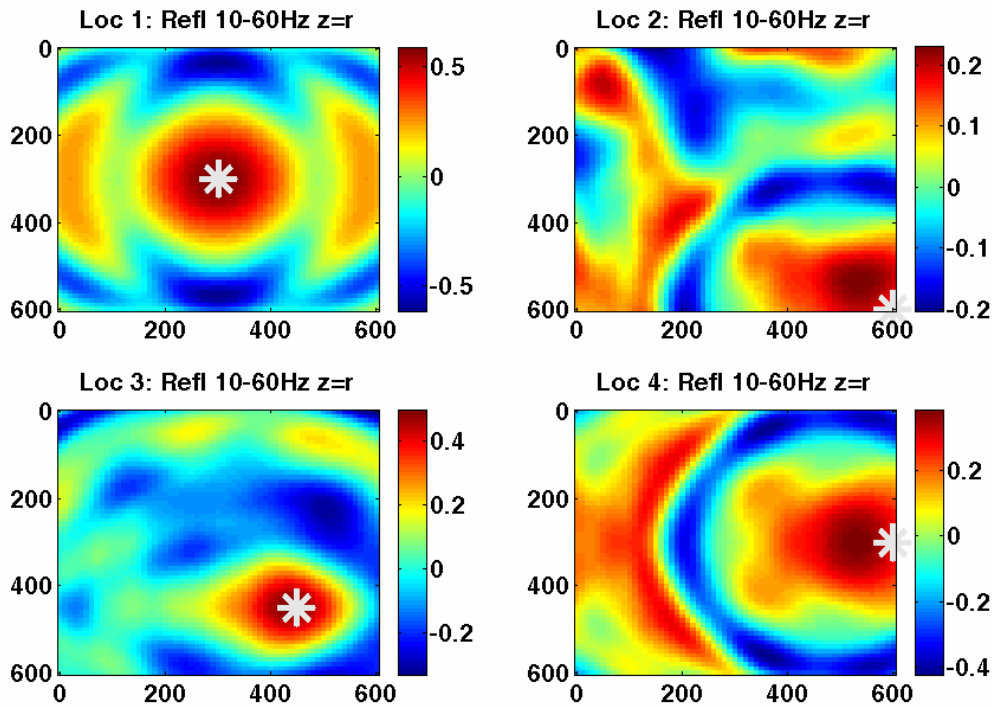
Figure 45. Similar to Figure 44 except that surface wave strength is now $a_{relsurf} = 100$.
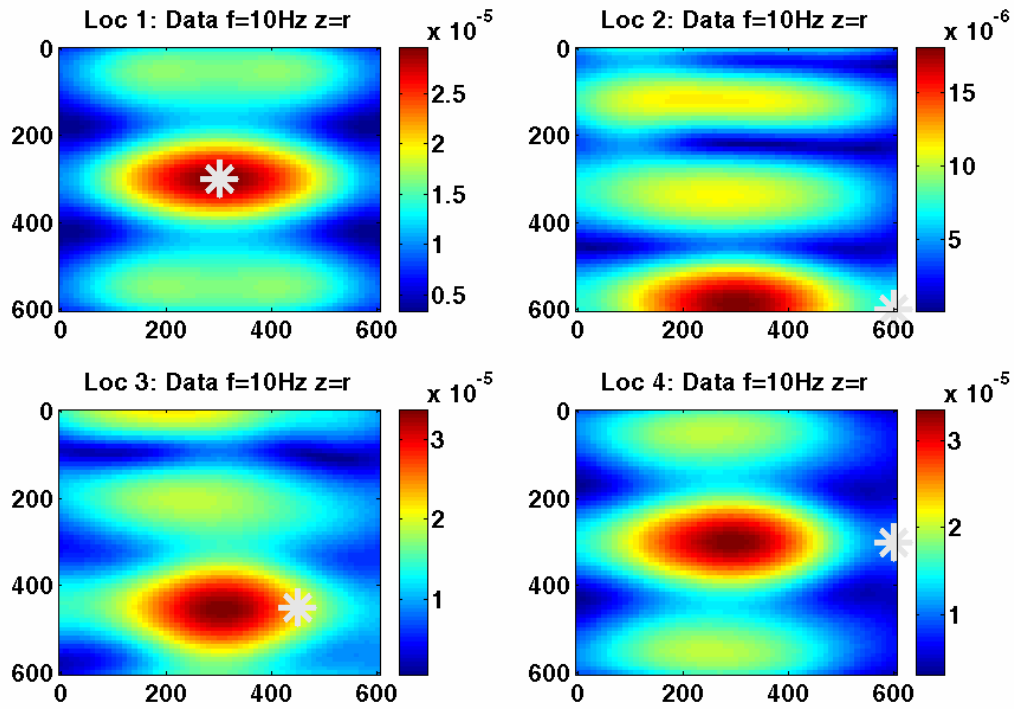
Figure 46. For the case summarized in Figure 43 ($a_{relsurf} = 10.$), this is 10 Hz data at the reflector.
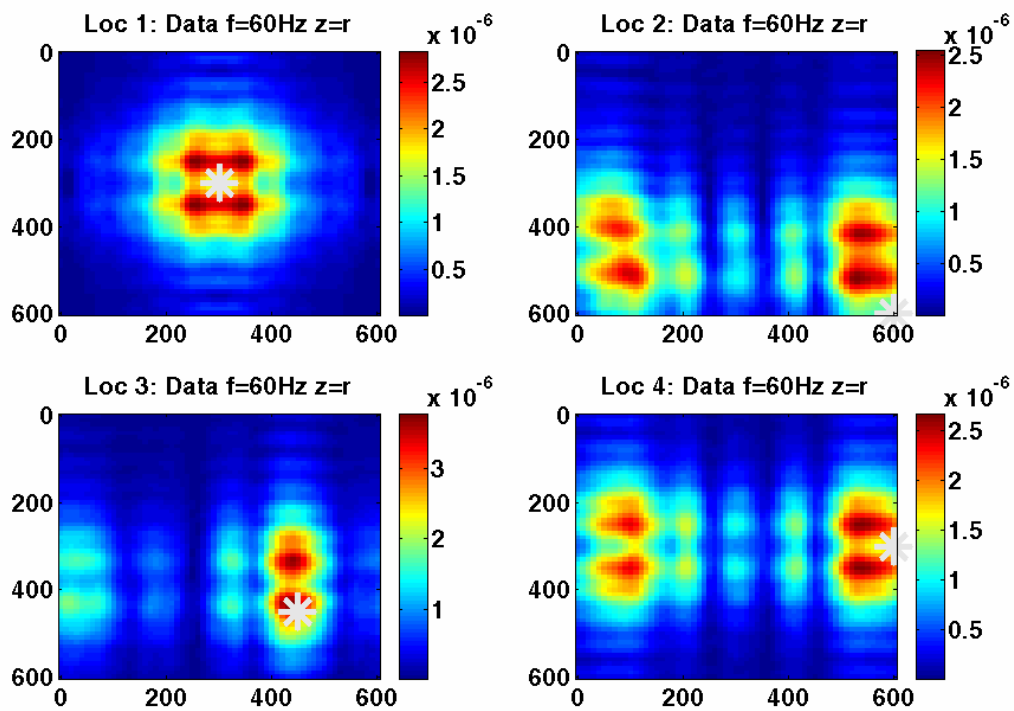
Figure 47. Similar to Figure 46 except that this is the 60 Hz data at the reflector.
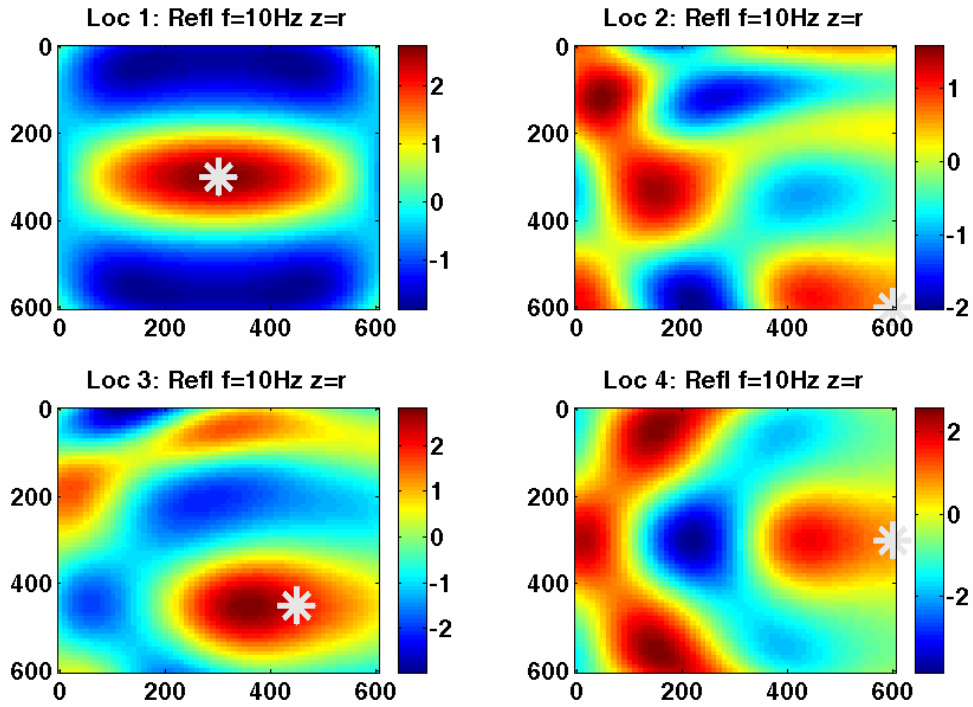
Figure 48. The reflectivity estimate at 10 Hz made from the data of Figure 46 using a deconvolution imaging condition.
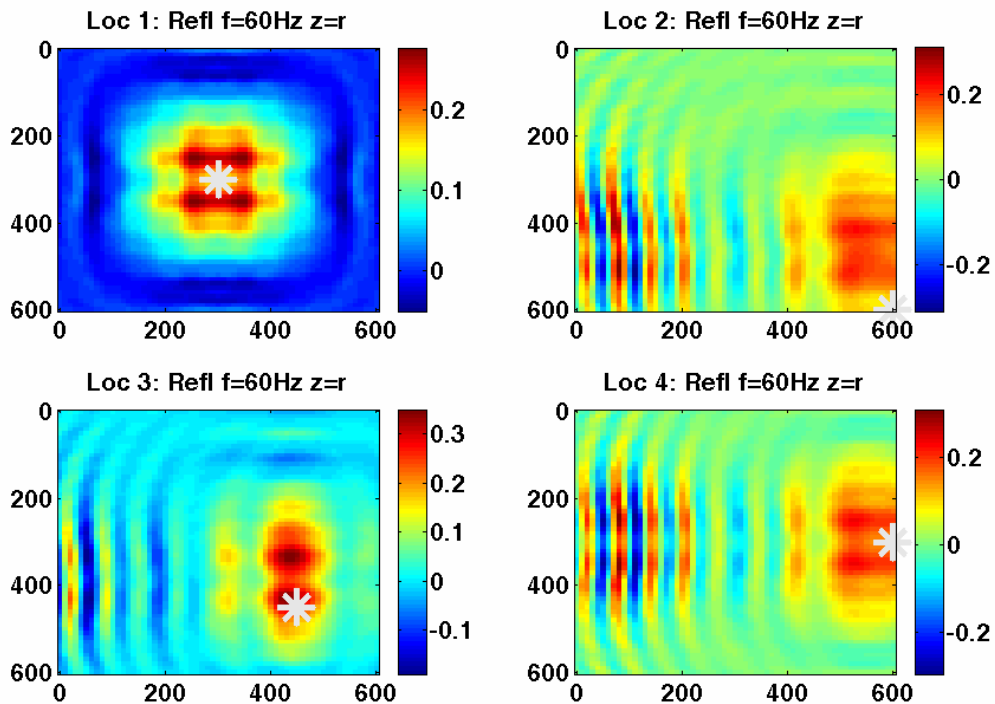

Figure 49. The reflectivity estimate at 60 Hz made from the data of Figure 47 using a deconvolution imaging condition.
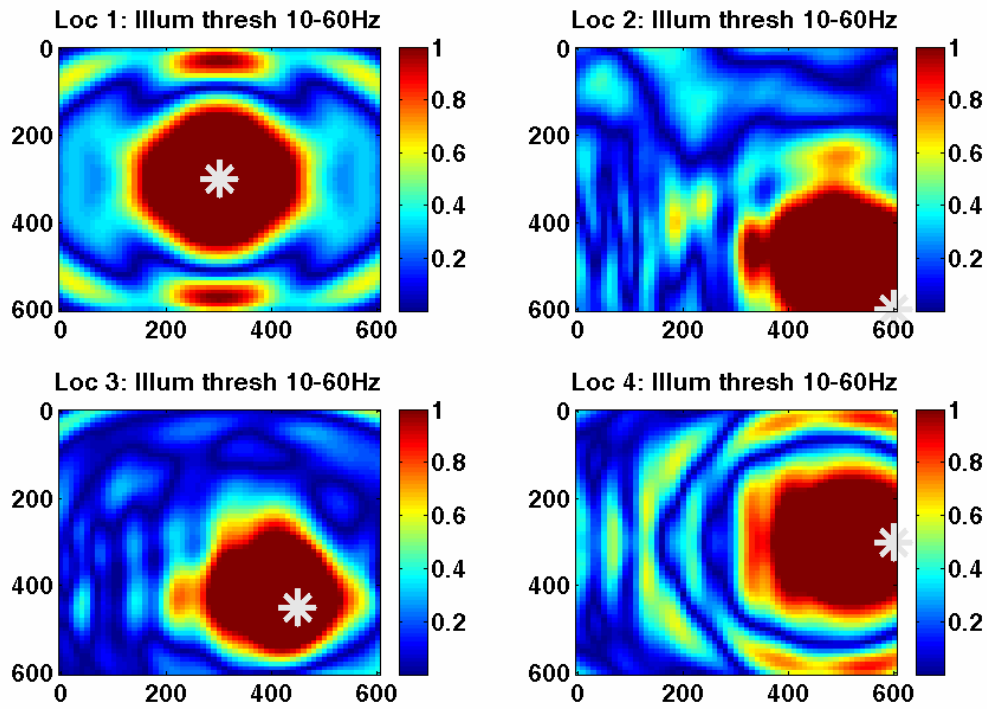
Figure 50. The illumination estimate $I_{r;j}$ made from the broadband reflectivity estimate of Figure 43.
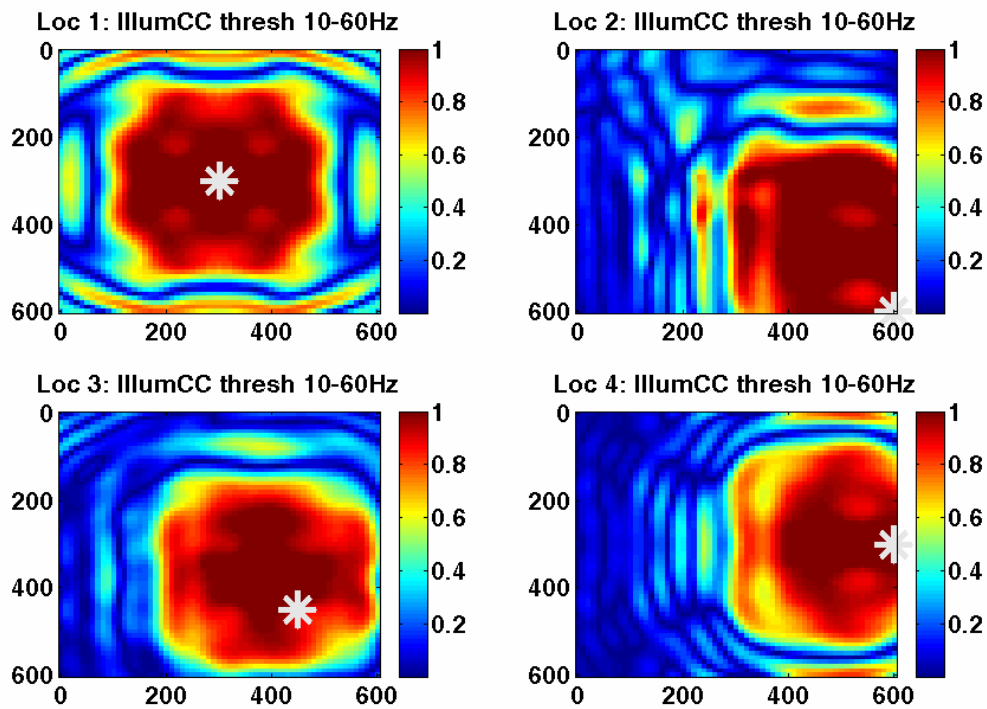
Figure 51. Similar to Figure 50 except that the illumination estimate $I_{cc;j}$ is shown.

CONCLUSIONS

A flexible and realistic set of Matlab scripts has been developed to model 3D prestack depth migration with realistic land acquisition geometries and noise effects. Both PP and PS imaging can be simulated. Two alternative calculations of illumination compensation has been explored. It is intended for these scripts to serve as guides in assessing acquisition geometry designs. Clear evidence of acquisition footprint effects is present in all simulations, even those with little or no noise. Though the reduced receiver and source lattices are severely aliased, they compensate for one another because of the orthogonal line geometry. To some extent the aliasing caused by the course line spacing it therefore overcome. Illumination compensation of prestack migrated volumes seems to reduce the aperture effect but can exaggerated other footprint artifacts. It may be that a better choice of the illumination threshold would improve things. This technique seems effective in modeling spatial aliasing, the effects of finite bandwidth, random noise levels, coherent noise levels, and source-receiver spacings.

ACKNOWLEDGEMENTS

REFERENCES:

Rickett, J.E., 2003, Illumination-based normalization for wave-equation depth migration: **GEOPHYSICS**, Soc. of Expl. Geophys., **68,** 1371-1379.

Vermeer, G. J. O., 1990, Seismic Wavefield Sampling, Seismic wavefield sampling: Soc. of Expl. Geophys., 120.

Vermeer, G. J. O., 1998, 3-D symmetric sampling: **GEOPHYSICS**, Soc. of Expl. Geophys., **63,** 1629-1647.